

POLITECNICO DI TORINO

Facoltà di Ingegneria  
Corso di Laurea in Ingegneria Aerospaziale

Tesi di Laurea Magistrale

# Escape trajectories exploiting multiple lunar gravity assists



**Relatori:**

prof. Lorenzo Casalino  
prof. Michèle Lavagna

**Candidato:**

Maurizio VALESANI

ANNO ACCADEMICO 2017-2018



## Abstract

Taking advantage of a gravity assist manoeuvre is a common strategy to achieve generally high  $\Delta V$  without resorting to the consumption of propellant – thus increasing the transportable payload mass –, as the gained energy is provided by the gravitational pull of a celestial body. In this instance, lunar gravity assists stand out as an extremely competitive alternative to direct escapes when evasion from Earth’s sphere of influence is considered.

This study is aimed at investigating the opportunity provided by a multiple-gravity-assist-aided escape, by examining the possible moon-to-moon trajectories allowing two consecutive gravity assist manoeuvres and the effect on the escape orbit, with the intent to link the characteristics of said final orbit – heliocentric flight-path angle and declination – to the maximum achievable specific mechanical energy (i.e. the obtainable escape velocity).

After a brief introduction, the mathematical models adopted throughout the dissertation will be presented; a description of the methodology for the analysis of moon-to-moon orbits and lunar gravity assists will then be introduced in a dedicated chapter, followed by a presentation of the obtained results. The final chapter consists of conclusive remarks, in addition to the difficulties faced during the work activity and a brief discussion about possible future developments of the present study.



# Contents

<b>1</b>	<b>Introduction</b>	<b>1</b>
<b>2</b>	<b>Mathematical model</b>	<b>5</b>
2.1	The $N$ -body problem . . . . .	5
2.2	The 2-body problem . . . . .	9
2.3	Constants of the motion . . . . .	11
2.3.1	Specific angular momentum . . . . .	11
2.3.2	Specific mechanical energy . . . . .	12
2.4	Equation of the trajectory . . . . .	14
2.5	The circular restricted 3-body problem . . . . .	15
2.6	Gravity assist . . . . .	17
2.6.1	The patched-conics approximation . . . . .	17
2.6.2	Lunar gravity assist . . . . .	18
<b>3</b>	<b>Analysis</b>	<b>23</b>
3.1	Solar-perturbed moon-to-moon transfer . . . . .	23
3.2	Moon-to-escape lunar gravity assist . . . . .	27
3.2.1	Lunar gravity assist evaluation . . . . .	27
3.2.2	Maximum $C3$ , given heliocentric flight-path angle and declination . . . . .	33
<b>4</b>	<b>Results</b>	<b>35</b>
4.1	Moon-to-moon leg . . . . .	35
4.1.1	Outbound-inbound . . . . .	35
4.1.2	Inbound-inbound . . . . .	36

4.2	Lunar gravity assist . . . . .	42
4.2.1	$C3(\gamma, \delta)$ maps . . . . .	42
4.2.2	$C3(\gamma)$ for given $\delta$ . . . . .	56
4.2.3	Global results . . . . .	68
<b>5</b>	<b>Conclusions</b>	<b>73</b>
5.1	Conclusions . . . . .	73
5.2	Future work . . . . .	74

# List of Tables

4.1	Ranges (in $^{\circ}$ ) for $\alpha$ and $\theta_{SC}$ for oi families. . . . .	36
4.2	Ranges (in $^{\circ}$ ) for $\alpha$ and $\theta_{SC}$ for ii families. . . . .	38
4.3	Maximum $C3$ [ $km^2/s^2$ ] achievable for each family. . . . .	43
4.4	Minimum guaranteed $C3$ achievable for each family. . . . .	43



# List of Figures

2.1	The $N$ -body problem. . . . .	8
2.2	Relative motion of 2 bodies. . . . .	10
2.3	Zenit and flight-path angle. . . . .	13
2.4	The 3-body problem in an inertial reference. . . . .	16
2.5	Lunar gravity assist manoeuvre schema. . . . .	20
2.6	Components of $\mathbf{V}_\infty$ expressed via pump ( $p$ ) and crank ( $k$ ) angles. . . . .	21
3.1	Problem schema. . . . .	24
3.2	Geometrical schema for escape orbit. . . . .	32
3.3	Heliocentric flight-path angle ( $\gamma_H$ ) and declination ( $\delta_H$ ) for the spacecraft's velocity after the lunar gravity assist. . . . .	33
4.1	Outbound-inbound orbits. . . . .	37
4.2	Inbound-inbound orbits. . . . .	39
4.3	Range of $\alpha$ that allow a rendezvous for oi and ii families. . . . .	40
4.4	Range of $\theta$ that allow a rendezvous for oi and ii families. . . . .	41
4.5	Maximum $C3$ achievable for each family. . . . .	43
4.6	$C3(\gamma, \delta)$ map for $Aoi$ family. . . . .	45
4.7	$C3(\gamma, \delta)$ map for $Aii$ family. . . . .	45
4.8	$C3(\gamma, \delta)$ map for $Boi$ family. . . . .	47
4.9	$C3(\gamma, \delta)$ map for $Bii$ family. . . . .	47
4.10	$C3(\gamma, \delta)$ map for $Coi$ family. . . . .	49
4.11	$C3(\gamma, \delta)$ map for $Cii$ family. . . . .	49
4.12	$C3(\gamma, \delta)$ map for $Doi$ family. . . . .	51
4.13	$C3(\gamma, \delta)$ map for $Dii$ family. . . . .	51

---

4.14 $C3(\gamma, \delta)$ map for $Eoi$ family. . . . .	53
4.15 $C3(\gamma, \delta)$ map for $Eii$ family. . . . .	53
4.16 $C3(\gamma, \delta)$ map for $Foi$ family. . . . .	55
4.17 $C3(\gamma, \delta)$ map for $Fii$ family. . . . .	55
4.18 $C3(\gamma)$ for fixed $\delta$ , $Aoi$ family . . . . .	57
4.19 $C3(\gamma)$ for fixed $\delta$ , $Aii$ family . . . . .	57
4.20 $C3(\gamma)$ for fixed $\delta$ , $Boi$ family . . . . .	59
4.21 $C3(\gamma)$ for fixed $\delta$ , $Bii$ family . . . . .	59
4.22 $C3(\gamma)$ for fixed $\delta$ , $Coi$ family . . . . .	61
4.23 $C3(\gamma)$ for fixed $\delta$ , $Cii$ family . . . . .	61
4.24 $C3(\gamma)$ for fixed $\delta$ , $Doi$ family . . . . .	63
4.25 $C3(\gamma)$ for fixed $\delta$ , $Dii$ family . . . . .	63
4.26 $C3(\gamma)$ for fixed $\delta$ , $Eoi$ family . . . . .	65
4.27 $C3(\gamma)$ for fixed $\delta$ , $Eii$ family . . . . .	65
4.28 $C3(\gamma)$ for fixed $\delta$ , $Foi$ family . . . . .	67
4.29 $C3(\gamma)$ for fixed $\delta$ , $Fii$ family . . . . .	67
4.30 $C3_{max}(\gamma, \delta)$ . . . . .	69
4.31 $C3_{max}(\gamma)$ for fixed $\delta$ . . . . .	69
4.32 Minimum $C3_{max}(\gamma)$ varying with $\delta$ . . . . .	70
4.33 Maximum $C3_{max}(\gamma)$ varying with $\delta$ . . . . .	71
4.34 Minimum and maximum $C3_{max}(\gamma)$ varying with $\delta$ . . . . .	71

# Chapter 1

## Introduction

When designing an interplanetary mission, the definition of the escape trajectory from Earth's sphere of influence – i.e. the spheroidal region of space surrounding Earth where the main source of gravitational attraction is Earth itself – and the associated manoeuvre is a key aspect, as it is tasked to inject the spacecraft on the desired heliocentric orbit. Depending on the scope of the mission, different escape strategies can be adopted. Such choice is paramount, due to the influence it bears on the cost of the mission in terms of propellant required, which directly impacts the payload mass that can be transported. Typical escape strategies are:

- direct escape – requiring a high-thrust propulsion system, thus needing chemical propellants, a direct escape consists of a single-impulse manoeuvre bringing the spacecraft on an hyperbolic orbit, which is then travelled upon until the escape conditions, meaning the desired hyperbolic excess velocity, are met;
- Oberth manoeuvre (powered flyby) – within the context of minimizing gravitational losses, this strategy consists of two single-impulse manoeuvres. The first one is aimed at reducing the speed of the spacecraft, achieving an Hohmann transfer in order to move closer to the main body. Once the now lowered periastron is reached, the second impulse is given, injecting the spacecraft on an hyperbolic escape orbit, similar to the one of the direct escape. Since the second impulse

is given at higher speed – lower altitude –, gravitational losses are reduced and, provided that the desired escape velocity is at least equal to  $\sqrt{2}$  times the starting circular velocity, the increase in  $\Delta V$  associated to the first impulse is compensated, leading to an inferior global  $\Delta V$  required and a more convenient escape. Relying upon two impulse manoeuvres, an Oberth escape is feasible when chemical propulsion is used;

- low-thrust escape – when the spacecraft is equipped with an electric propulsion system, impulsive manoeuvres are not feasible any more, due to the low achievable acceleration values, generally in the range of  $1 \text{ mm/s}^2$ . Thus, the escape consists of a continuous applied thrust, slightly directed towards the main body in order to reduce gravitational losses at the cost of facing misalignment losses, leading the spacecraft to follow a spiral orbit. While exploiting the higher specific impulse of electric propulsion compared to chemical propulsion, the drawback of such an escape strategy is associated to its duration, that can reach several years;
- gravity assist – unrelated to the necessity of using a specific propellant, either chemical or electrical, a gravity assist exploits the exchange of momentum between the spacecraft and the main body to rotate the spacecraft velocity in order to gain a  $\Delta V$ . While it is commonly used for escapes – and, in this context, it will be the focus of this thesis – as it does not require the consumption of propellant, it is often resorted to for non-escape trajectories, due to its convenience.

The aim of the present work is to investigate the possibility of exploiting multiple gravity assist manoeuvres within the moon's sphere of influence to achieve an escape from Earth's gravitational pull. Consequently, possible moon-to-moon transfers allowing two consecutive gravity assist manoeuvres have been studied, along with the second gravity assist itself that provides the escape conditions; the first flyby has been considered in the form of the starting conditions for the spacecraft. Chapter 2 of this thesis is focused on

---

the mathematical models exploited for the study. First, the N-body problem and its specialization for two and three bodies, which have been used for the determination of the coplanar moon-to-moon transfer between the two gravity assist manoeuvres, is presented, followed by an explanation of the rationale behind the gravity assist itself. Chapter 3 is dedicated to the performed analysis of both topics, with a detailed description of the specifically developed algorithms for both the inter-gravity assist trajectory and the evaluation of the escape conditions based on the desired heliocentric flight-path angle and declination of the spacecraft velocity vector. The main results are outlined in chapter 4, where the identified moon-to-moon transfers are presented, together with the maps linking flight-path angle and declination to the associated characteristic energy – and, thus, escape velocity. Conclusive considerations and remarks, as well as a discussion on the main difficulties that have been faced during this study and the possible future developments, are included in chapter 5.



# Chapter 2

## Mathematical model

In order to determine the desired trajectories, the mathematical model of the circular restricted three body problem has been used. The general  $N$ -body problem will first be presented, and it will be then specialized to the problem of two and three bodies, with a brief discussion on the constants of motion. Section 2.6 will focus on the mathematical model adopted for the analysis of the gravity assist manoeuvre, describing the manoeuvre itself after a presentation of the patched-conics approximation.

### 2.1 The $N$ -body problem

The aim of the  $N$ -body problem model is to describe the mutual gravitational interaction among  $N$  masses in order to determine their motion. Therefore, the nature of such interaction needs to be explained, which can be done by referring to Newton's law of universal gravitation, presented in his *Philosophiæ Naturalis Principia Mathematica* in 1686 [8].

***Newton's law of universal gravitation***

*Any two bodies attract one another with a force along their joining line which is proportional to the product of their masses and inversely proportional to the square of their distance.*

This law can be expressed mathematically in vector notation<sup>1</sup>.

$$\mathbf{F}_g = -G \frac{mM}{r^2} \frac{\mathbf{r}}{r} \quad (2.1)$$

Here  $\mathbf{F}_g$  represents the force that the body of mass  $M$  applies onto the body of mass  $m$ , while  $\mathbf{r}$  is the position vector of  $m$  relative to  $M$ .  $G$  is a constant coefficient, the universal gravitational constant, which has the value  $G = 6.67259 \cdot 10^{-11} \text{m}^3 / (\text{kg} \cdot \text{s}^2)$ . The negative sign that precedes the second member highlights the attractive nature of the gravitational force.

Finally, it is worth mentioning Newton's third law.

***Newton's third law***

*Every force exerted on object B by another object A, object B will instantly exert another force with same magnitude but opposite direction on object A.*

Consequently, the force on  $m$  generated by  $M$  has the same intensity as the one on  $M$  caused by  $m$ , but opposite direction.

We shall assume a system composed of  $n$  masses ( $m_1, m_2 \dots m_i \dots m_n$ ), the coordinates of which are defined in an inertial reference system ( $X, Y, Z$ ) by position vectors ( $\mathbf{r}_1, \mathbf{r}_2 \dots \mathbf{r}_i \dots \mathbf{r}_n$ ), as shown in figure 2.1. In order to determine the motion of the  $i^{\text{th}}$  body using Newton's second law, it is necessary to identify the combined force acting on  $m_i$ .

***Newton's second law***

*The rate of change of momentum of an object is proportional to the force impressed on it and is the same direction as that force.*

Equation 2.2 is the mathematical expression of such law.

$$\sum \mathbf{F} = \frac{d}{dt} (m_i \dot{\mathbf{r}}_i) \quad (2.2)$$

The resulting force acting on  $m_i$  can be expressed as

$$\sum \mathbf{F} = \mathbf{F}_g + \mathbf{F}_{\text{other}}$$

<sup>1</sup>The convention for which vectors are indicated by bold font while scalars with regular font will be adopted throughout this text.

Where  $\mathbf{F}_g$  is the global effect of gravitational forces, while  $\mathbf{F}_{other}$  includes all other kind of forces (such as thrust, perturbations, atmospheric drag or solar pressure).

It is to be noted how  $\mathbf{F}_g$  merges the gravitational effects of every mass in the system except from  $m_i$ . Thus, this term can be expressed exploiting equation 2.1, where  $\mathbf{r}_{ji}$  is the vector joining the  $j^{th}$  and the  $i^{th}$  masses.

$$\mathbf{F}_g = -Gm_i \sum_{\substack{j=1 \\ j \neq i}}^n \frac{m_j}{r_{ji}^3} \mathbf{r}_{ji} \quad (2.3)$$

Consequently, the equation describing the motion of the  $i^{th}$  body can be derived by expanding equation 2.2 into equation 2.4:

$$\ddot{\mathbf{r}}_i = -G \sum_{\substack{j=1 \\ j \neq i}}^n \frac{m_j}{r_{ji}^3} \mathbf{r}_{ji} + \frac{\mathbf{F}_{other}}{m_i} - \dot{\mathbf{r}}_i \frac{\dot{m}_i}{m_i} \quad (2.4)$$

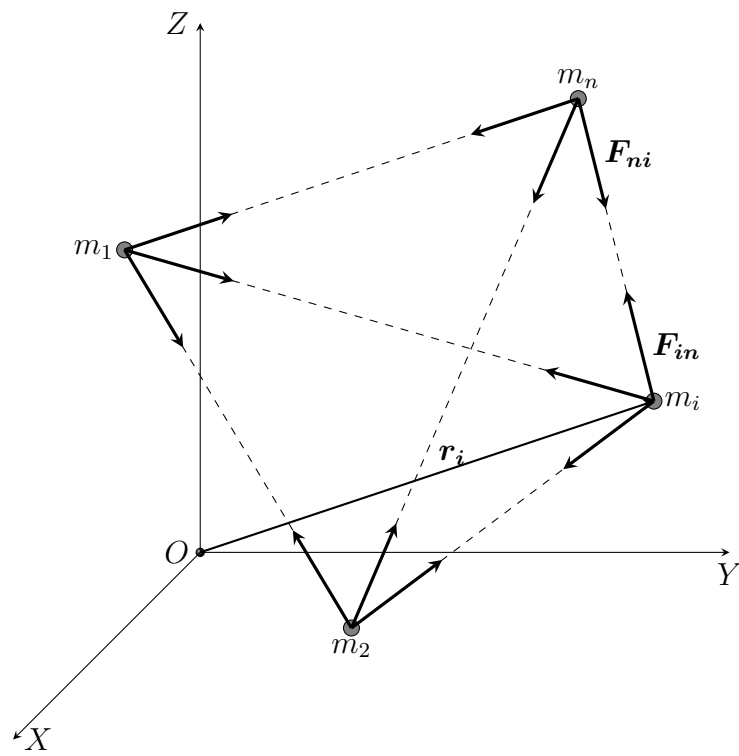
Due to the notable complexity hidden in the resolution of the  $N$ -body problem, simplifying hypotheses are introduced. While these assumptions make the problem no longer perfectly descriptive of the real phenomenon, they do not compromise the reliability of the results.

Thus, we shall assume the involved bodies to be uniform and spherical, in order to consider them punctiform, as well as constant in time (this second assumption is often quite accurate, e.g. when considering a satellite on a Newtonian orbit, i.e. with thrusters off); moreover, we shall assume no force other than the gravitational one is acting inside the system, allowing all kind of external perturbation to be ignored.

As a consequence,  $\mathbf{F}_{other}$  and  $\dot{m}_i$  are null, which simplifies equation 2.4.

$$\ddot{\mathbf{r}}_i = -G \sum_{\substack{j=1 \\ j \neq i}}^n \frac{m_j}{r_{ji}^3} \mathbf{r}_{ji} \quad (2.5)$$

Equation 2.5, however, describes the motion of the  $i^{th}$  body relatively to the inertial reference system, while the goal is usually to describe this motion relatively to another body (e.g. the motion of a satellite orbiting Earth or of

Figure 2.1: The  $N$ -body problem.

Earth orbiting the sun).

Consider, for example, to describe how  $m_2$  moves in relation to  $m_1$ . First, the equations of motion in the inertial reference system of both bodies need to be written.

$$\begin{cases} \ddot{\mathbf{r}}_1 = -G \sum_{j=2}^n \frac{m_j}{r_{j1}^3} \mathbf{r}_{j1} \\ \ddot{\mathbf{r}}_2 = -G \sum_{\substack{j=1 \\ j \neq 2}}^n \frac{m_j}{r_{j2}^3} \mathbf{r}_{j2} \end{cases} \quad (2.6)$$

Figure 2.1 shows how the position of body 2 in relation to body 1 can be expressed:

$$\mathbf{r}_{12} = \mathbf{r}_2 - \mathbf{r}_1 \quad (2.7)$$

Clearly, a similar equation links accelerations.

$$\ddot{\mathbf{r}}_{12} = \ddot{\mathbf{r}}_2 - \ddot{\mathbf{r}}_1 \quad (2.8)$$

As a consequence, subtracting equation for mass  $m_1$  from the other one yields equation 2.9, describing the motion of the secondary body around the main one.

$$\ddot{\mathbf{r}}_{12} = -G \sum_{\substack{j=1 \\ j \neq 2}}^n \frac{m_j}{r_{j2}^3} \mathbf{r}_{j2} + G \sum_{j=2}^n \frac{m_j}{r_{j1}^3} \mathbf{r}_{j1} \quad (2.9)$$

Gathering the terms proportional to  $\mathbf{r}_{12}$  and highlighting how  $\mathbf{r}_{21} = -\mathbf{r}_{12}$ , equation 2.9 can be rewritten as:

$$\ddot{\mathbf{r}}_{12} = -G \frac{m_1 + m_2}{r_{12}^3} \mathbf{r}_{12} - G \sum_{j=3}^n m_j \left( \frac{\mathbf{r}_{j2}}{r_{j2}^3} - \frac{\mathbf{r}_{j1}}{r_{j1}^3} \right) \quad (2.10)$$

## 2.2 The 2-body problem

Even introducing the simplifying hypotheses described above, though, the solution to the  $N$ -body problem has defied solution in its present form, since

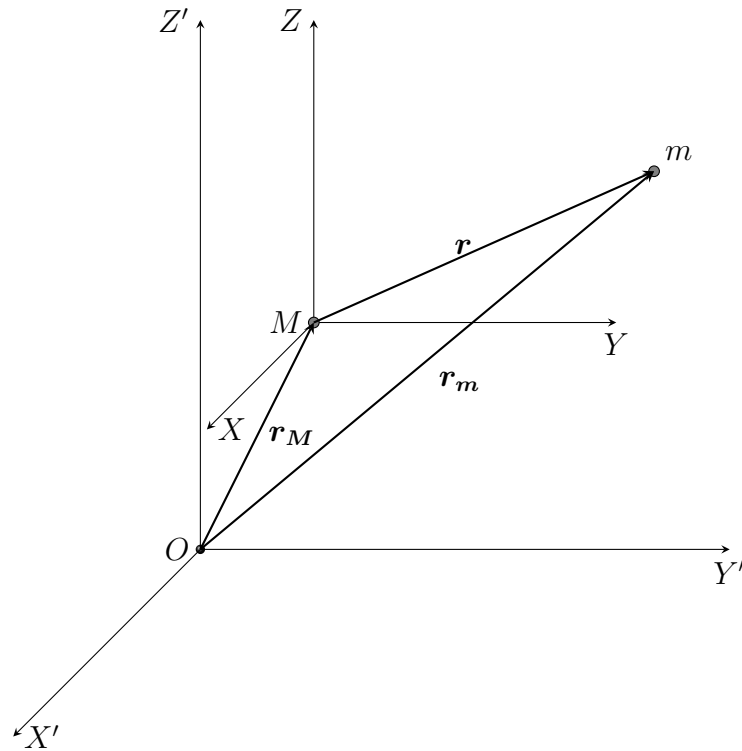


Figure 2.2: Relative motion of 2 bodies.

equation 2.10 is a second order, non-linear, vector, differential equation of motion, which requires numerical integration to identify a solution. Nonetheless, it is possible to find an analytic solution to such problem by limiting the number of bodies involved to two: a main body  $M$  and a secondary one  $m$  orbiting the first. If the mass of the secondary body is notably inferior to that of the primary one, the hypothesis of restriction can be introduced, with the consequent relation  $m \ll M$ .

Consider  $(X', Y', Z')$  an inertial reference system and  $(X, Y, Z)$  a non-rotating reference system parallel to the previous one and the origin of which coincides with the position of the main body. Furthermore, consider  $\mathbf{r}_M$  and  $\mathbf{r}_m$  the position vectors of the two bodies in the inertial system, and  $\mathbf{r}$  the position vector of  $m$  in  $(X, Y, Z)$ , as shown in figure 2.2.

Equation 2.10 can then be rewritten.

$$\ddot{\mathbf{r}} = -G \frac{m + M}{r^3} \mathbf{r} \quad (2.11)$$

Thanks to the introduction of the hypothesis of restriction,  $m + M \simeq M$ . We shall also introduce the gravitational parameter  $\mu = GM$ , thus leading to equation 2.12.

$$\ddot{\mathbf{r}} = -\frac{\mu}{r^3} \mathbf{r} \quad (2.12)$$

## 2.3 Constants of the motion

In order to obtain the equation of the trajectory by integrating the equation of motion, it is first necessary to describe some constants that characterize orbital motion itself. First, specific angular momentum  $h$  will be introduced, which will then be followed by specific mechanical energy  $\mathcal{E}$ .

### 2.3.1 Specific angular momentum

It is possible to demonstrate how the angular momentum characterizing an orbiting body maintains its magnitude and direction when no force other than the gravitational one acts on the system.

First, both terms of equation 2.12 can be cross multiplied to the left by  $\mathbf{r}$ , thus yielding:

$$\mathbf{r} \times \ddot{\mathbf{r}} = -\mathbf{r} \times \frac{\mu}{r^3} \mathbf{r} \quad (2.13)$$

Since it is known that  $\mathbf{r} \times \mathbf{r} = 0$ , since a vector will always be parallel to itself, the second term then disappears, which leads to:

$$\mathbf{r} \times \ddot{\mathbf{r}} = 0 \quad (2.14)$$

It is to be noted, though, that:

$$\frac{d}{dt} (\mathbf{r} \times \dot{\mathbf{r}}) = \mathbf{r} \times \ddot{\mathbf{r}} + \dot{\mathbf{r}} \times \dot{\mathbf{r}} \quad (2.15)$$

Where  $\dot{\mathbf{r}} \times \dot{\mathbf{r}} = 0$  for the same reason stated above. Thus, it can be inferred that  $\mathbf{r} \times \dot{\mathbf{r}} = \text{const.}$ , as its derivative is null. But  $\dot{\mathbf{r}} = \mathbf{V}$  is the velocity vector. The expression  $\mathbf{r} \times \mathbf{V}$  is then a constant of the motion and is called specific angular momentum  $\mathbf{h}$ .

Having demonstrated that  $\mathbf{h}$  is constant leads to an extremely relevant conclusion: since the angular momentum is the cross product of  $\mathbf{r}$  and  $\mathbf{V}$ , it will be a vector perpendicular to both; but, due to its being constant in magnitude and direction,  $\mathbf{r}$  and  $\mathbf{V}$  will always lie on the same plane. Therefore, Newtonian orbits are confined to a plane, which we shall refer to as orbital plane.

Finally, it is possible to link the magnitude of  $\mathbf{h}$  with the direction of  $\mathbf{V}$ , via the flight-path angle  $\varphi$  (i.e. the angle between the velocity vector and the local radial). From figure 2.3 it is clear how the zenith angle ( $\gamma$ ) and the flight-path angle are complementary. It can then be written that:

$$h = rV \cos \varphi \quad (2.16)$$

### 2.3.2 Specific mechanical energy

In addition to specific angular momentum, also the specific mechanical energy  $\mathcal{E}$  (i.e. the sum of potential and kinetic energy per unit mass) is a constant of motion characterizing each orbit.

To demonstrate this property of mechanical energy it is first necessary to dot multiply equation 2.12 by  $\dot{\mathbf{r}}$ :

$$\dot{\mathbf{r}} \cdot \ddot{\mathbf{r}} + \dot{\mathbf{r}} \cdot \frac{\mu}{r^3} \mathbf{r} = 0 \quad (2.17)$$

That can be rewritten as:

$$\dot{r}\ddot{r} + \dot{r} \frac{\mu}{r^2} = 0 \quad (2.18)$$

It can be noted that  $\dot{r} = V$  and that:

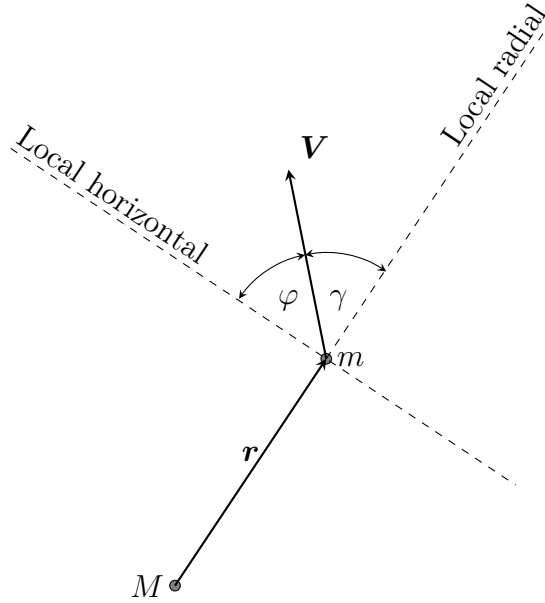


Figure 2.3: Zenit and flight-path angle.

$$\begin{cases} V\dot{V} = \frac{d}{dt} \left( \frac{V^2}{2} \right) \\ \dot{r} \frac{\mu}{r^2} = \frac{d}{dt} \left( -\frac{\mu}{r} \right) \end{cases} \quad (2.19)$$

Thus, it is possible to write:

$$\frac{d}{dt} \left( \frac{V^2}{2} - \frac{\mu}{r} \right) = 0 \quad (2.20)$$

Which leads to the desired equation.

$$\mathcal{E} = \frac{V^2}{2} - \frac{\mu}{r} + C = \text{const.} \quad (2.21)$$

Where  $C$  is a constant term coming from the integration of equation 2.20.  $\frac{V^2}{2}$  is clearly the kinetic energy per unit mass, as it expresses the energy contribution due to motion. On the other hand,  $-\frac{\mu}{r}$  is the potential energy per unit mass due to the gravitational field, depending only on the position of the orbiting body and the mass of the main body. Finally,  $C$  is a constant of integration and thus its value is arbitrary; it can be then set equal to zero

to simplify equation 2.21, which is equivalent to choosing the zero reference for potential energy at infinity.

## 2.4 Equation of the trajectory

Having identified the constants that characterize orbital motion, it is now finally possible to obtain the trajectory equation for the 2-body problem, by integrating twice equation 2.12. In order to do so, however, it is easier to manipulate the starting equation to identify derivatives instead of integrating it as it is.

First, equation 2.12 can be cross multiplied by  $\mathbf{h}$ , the specific angular momentum vector:

$$\ddot{\mathbf{r}} \times \mathbf{h} = \frac{\mu}{r^3} (\mathbf{h} \times \mathbf{r}) \quad (2.22)$$

It is easy to identify a derivative in the left side of equation 2.22, since

$$\frac{d}{dt} (\dot{\mathbf{r}} \times \mathbf{h}) = (\ddot{\mathbf{r}} \times \mathbf{h}) + (\dot{\mathbf{r}} \times \dot{\mathbf{h}}) \quad (2.23)$$

As far as the right side is concerned, it can be turned into the time rate of change of another vector quantity:

$$\begin{aligned} \frac{\mu}{r^3} (\mathbf{h} \times \mathbf{r}) &= \frac{\mu}{r^3} (\mathbf{r} \times \mathbf{V}) \times \mathbf{r} = \\ &= \frac{\mu}{r^3} [\mathbf{V} (\mathbf{r} \cdot \mathbf{r}) - \mathbf{r} (\mathbf{r} \cdot \mathbf{V})] = \\ &= \frac{\mu}{r} \mathbf{V} - \frac{\mu \dot{r}}{r^2} \mathbf{r} = \\ &= \mu \frac{d}{dt} \left( \frac{\mathbf{r}}{r} \right) \end{aligned} \quad (2.24)$$

It is then possible to rewrite equation 2.12 as

$$\frac{d}{dt} (\dot{\mathbf{r}} \times \mathbf{h}) = \mu \frac{d}{dt} \left( \frac{\mathbf{r}}{r} \right) \quad (2.25)$$

Integration of equation 2.25 yields

$$\dot{\mathbf{r}} \times \mathbf{h} = \mu \frac{\mathbf{r}}{r} + \mathbf{B} \quad (2.26)$$

Where  $\mathbf{B}$  is a vector constant originated by the integration process. The second step consists of dot multiplying equation 2.26 by  $\mathbf{r}$ :

$$\mathbf{r} \cdot \dot{\mathbf{r}} \times \mathbf{h} = \mu \frac{\mathbf{r} \cdot \mathbf{r}}{r} + \mathbf{r} \cdot \mathbf{B} \quad (2.27)$$

That, by means of vector identities and defining  $\nu$  as the angle between  $\mathbf{B}$  and  $\mathbf{r}$ , can be rewritten as

$$h^2 = \mu r + r B \cos \nu \quad (2.28)$$

Solving for  $r$  leads to the trajectory equation.

$$r = \frac{\frac{h^2}{\mu}}{1 + \frac{B}{\mu} \cos \nu} \quad (2.29)$$

It is to be noted that equation 2.29 coincides with the equation of a conic section written in polar coordinates with its origin in one of the foci.

$$r = \frac{p}{1 + e \cos \nu} \quad (2.30)$$

Where  $p$  is the semilatus rectum and  $e$  the eccentricity, while  $\nu$ , just like in equation 2.29, is the angle between the point of the conic closest to the focus (called periastron when orbits are considered) and  $\mathbf{r}$ .

## 2.5 The circular restricted 3-body problem

To describe the orbital motion of the spacecraft between the two manoeuvres of lunar gravity assist, the approximation introduced by the 2-body model is, however, too restrictive, since it would ignore the notably relevant role played by the sun. Thus, it is necessary to adopt a different and more complex model including also the sun as well as Earth and the spacecraft, to avoid excessive imprecision in the solution. The price to be paid for this increase in complexity is the impossibility to identify an analytical solution. It is nonetheless possible to introduce some assumptions, in order to slightly

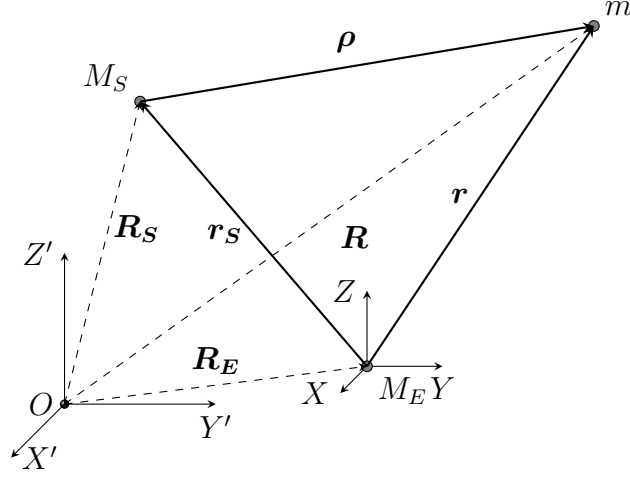


Figure 2.4: The 3-body problem in an inertial reference.

reduce the complexity of the problem without sacrificing accuracy.

We shall then introduce the model of the circular restricted 3-body problem. Of the three masses considered, only two are effectively taken into account during the calculations, as the third one  $m$  (in this case, the one corresponding to the spacecraft) is negligible. Along this hypothesis of restriction is the assumption that the two main bodies ( $m_1$  and  $m_2$ ) move on a circular orbit around their shared centre of mass. Let us consider the case for the Earth-Sun-spacecraft system. Figure 2.4 shows a schema for the 3-body model.

To write the vector equation describing the motion of the spacecraft relative to Earth, the gravitational effect of the three bodies needs to be expressed using equation 2.1 in the inertial reference frame first.

$$\begin{cases} m\ddot{\mathbf{R}} = -G\frac{mM_E}{r^2}\frac{\mathbf{r}}{r} - G\frac{mM_S}{\rho^2}\frac{\boldsymbol{\rho}}{\rho} & \text{for the spacecraft} \\ M_E\ddot{\mathbf{R}}_E = G\frac{M_Em}{r^2}\frac{\mathbf{r}}{r} + G\frac{M_EM_S}{r_S^2}\frac{\mathbf{r}_S}{r_S} & \text{for Earth} \\ M_S\ddot{\mathbf{R}}_S = -G\frac{M_SM_E}{r_S^2}\frac{\mathbf{r}_S}{r_S} + G\frac{M_Sm}{\rho^2}\frac{\boldsymbol{\rho}}{\rho} & \text{for the Sun} \end{cases} \quad (2.31)$$

By subtracting from the equation for the spacecraft the one for Earth, consid-

ering that  $\mathbf{r} = \mathbf{R} - \mathbf{R}_E$ , and exploiting the restriction assumption introduced before ( $m \ll M_E, M_S$ ), the equation describing the motion of the spacecraft relative to Earth is obtained.

$$\ddot{\mathbf{r}} = -G \frac{M_E}{r^3} \mathbf{r} - GM_S \left( \frac{\boldsymbol{\rho}}{\rho^3} + \frac{\mathbf{r}_S}{r_S^3} \right) \quad (2.32)$$

The trajectory solution for vector equation 2.32 can only be found via numerical integration (since it is not possible to identify an analytical solution like for the 2-body problem), transforming it into a system of six first-order differential equations.

## 2.6 Gravity assist

Commonly used as a manoeuvre for interplanetary missions since it allows for a spacecraft to gain notable  $\Delta V$  without having to resort to expending valuable and heavy propellant, a gravity assist – or swing by – exploits the gravitational pull of a celestial body as a source of energy. A positive or negative  $\Delta V$  can be achieved by rotating the spacecraft's relative velocity to the body itself: such rotation causes the absolute velocity in the inertial reference frame to change, both in direction and magnitude, since it can be calculated as the vector sum of the spacecraft's relative speed and the speed of the mass around which the manoeuvre takes place.

The example of a lunar gravity (LGA) assist will be introduced to briefly explain the rationale behind this manoeuvre. Before, however, the patched-conic approximation shall be described.

### 2.6.1 The patched-conics approximation

During interplanetary missions, a spacecraft is mostly under the gravitational influence of the sun alone and perturbations introduced by other celestial bodies intervene only when the spacecraft itself is in their close proximity. Thus, it is possible to approximate the motion of an interplanetary spacecraft

by splitting it into different conic orbits around the various masses the gravitational pull of which is relevant, and patching them together at the edge of the spheres of influence, that can be defined as a spherical portions of space within which the attraction of a single body prevails. While clearly an unrealistic description of the real phenomenon as the transition from orbiting a body to another is a gradual process and does not happen instantaneously, results are sufficiently accurate for a preliminary evaluation of a space mission.

Hereafter, the definition of sphere of influence proposed by Laplace will be adopted. Considering for example the moon inside Earth's gravitational field, its sphere of influence is centred at the moon and has radius:

$$r_s = R_{E-M} \left( \frac{M_M}{M_E} \right)^{\frac{2}{5}} \quad (2.33)$$

It is to be noted how equation 2.33 depends on the two bodies under exam, particularly their distance and their masses.

The patched-conics approximation can prove extremely useful when dealing with manoeuvres in close proximity of a celestial body. Gravity assists, for example, can be evaluated within the sphere of influence of a body such as the moon, and all other gravitational effects and perturbations can be ignored during preliminary calculations.

### 2.6.2 Lunar gravity assist

We shall consider a spacecraft headed towards the moon, where a lunar gravity assist manoeuvre is to be performed. When the spacecraft reaches the edge of the moon's sphere of influence, the system can be described by the 2-body problem model, where Earth's satellite stands as the main body and the spacecraft as the orbiting one. Figure 2.5 shows a graphical representation of the following description, referred to the planar case for simplicity.

The spacecraft enters the lunar sphere of influence with a velocity  $\mathbf{V}_{S/C}^-$

relative to the Earth-centred reference: to obtain the spacecraft's velocity relative to the moon in order to describe the motion with the 2-body model, the moon's velocity itself needs to be subtracted from  $\mathbf{V}_{S/C}^-$ .

$$\mathbf{V}_{\infty}^- = \mathbf{V}_{S/C}^- - \mathbf{V}_M \quad (2.34)$$

It is important to highlight the angle formed by  $\mathbf{V}_M$  and  $\mathbf{V}_{\infty}^-$ , the pump angle before LGA ( $p^-$ ), since it is crucial in evaluating the effectiveness of the manoeuvre.

Once  $\mathbf{V}_{\infty}^-$  is known, it is possible to identify the orbit the spacecraft lies upon; since the edge of the sphere of influence can be approximated by  $r \rightarrow \infty$  and, in order to enter it,  $V_{\infty}^-$  must be greater than 0, the orbit must be an hyperbola and, as long as the periselene is higher than the moon radius and, thus, no impact with the moon occurs, the spacecraft travels along the orbit and escapes the sphere of influence with a relative velocity  $\mathbf{V}_{\infty}^+$ . At the escape  $V_{\infty}^- = V_{\infty}^+$  due to the conservation of mechanical energy:

$$\mathcal{E} = \frac{V_{\infty}^{-2}}{2} - \frac{\overset{0}{H}}{r} = \frac{V_{\infty}^{+2}}{2} - \frac{\overset{0}{H}}{r} \quad (2.35)$$

However, while the magnitude of  $\mathbf{V}_{\infty}$  remains constant, its direction is changed by an angle  $\delta = \pi - 2\phi$ , where  $\phi = \arccos(1/e)$  is the opening angle of the hyperbola of eccentricity  $e$  upon which the spacecraft lies. Consequently, the angle  $\mathbf{V}_{\infty}$  forms with  $\mathbf{V}_M$  is changed as well. Thus  $p^- \neq p^+$  and, therefore:

$$\mathbf{V}_{S/C}^+ = \mathbf{V}_M + \mathbf{V}_{\infty}^+ \neq \mathbf{V}_{S/C}^- \quad (2.36)$$

The gravity assist manoeuvre can then be exploited to accelerate or decelerate a spacecraft without having to resort to the use of thrusters. This apparently free  $\Delta V$  is originated from the conservation of angular momentum for the moon-spacecraft system. Being  $\mathbf{r}_s$  the radius of the lunar sphere of influence:

$$\Delta H = m r_s \Delta V - M_M r_s \Delta V_M = 0 \quad (2.37)$$

Thus, simplifying  $r_s$ :

$$\Delta V_M = \frac{m}{M_M} \Delta V \quad (2.38)$$

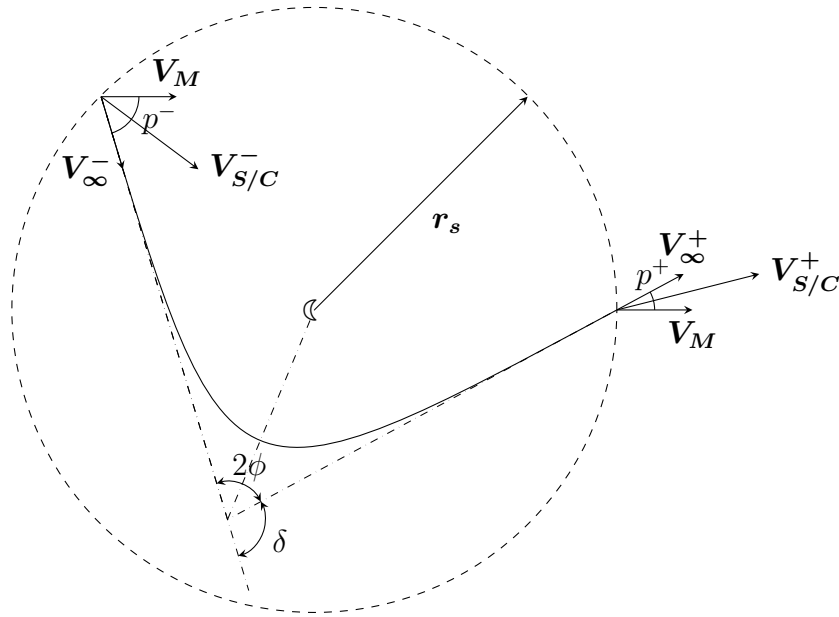


Figure 2.5: Geometrical schema for a generic lunar gravity assist manoeuvre.

However, since the spacecraft's mass is negligible compared to the mass of the moon,  $m \ll M_M$ , the effect on the moon's velocity is irrelevant.

In the more general case, gravity assists have an effect also on the inclination of the orbit, thus causing a  $\Delta i$  as well as a  $\Delta V$ . Along the pump angle, it is then necessary to introduce the crank angle to properly take into account the three components of the velocity vector: radial, tangential, and normal (figure 2.6).

$$\begin{cases} u_\infty = V_\infty \sin p \cos k \\ v_\infty = V_\infty \cos p \\ w_\infty = V_\infty \sin p \sin k \end{cases} \quad (2.39)$$

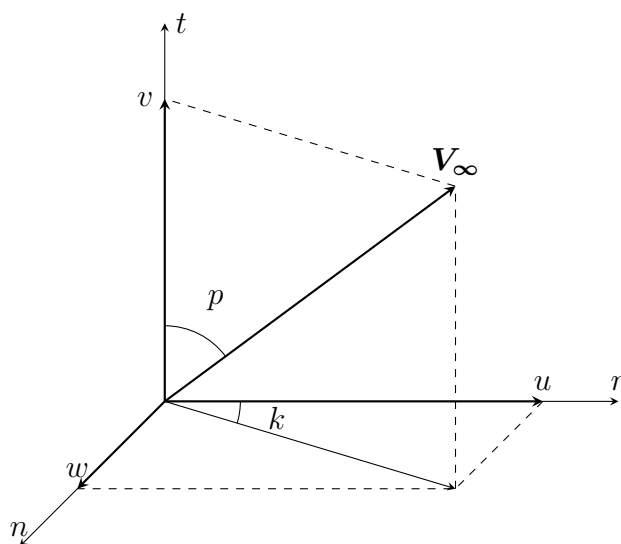


Figure 2.6: Components of  $\mathbf{V}_\infty$  expressed via pump ( $p$ ) and crank ( $k$ ) angles.



# Chapter 3

## Analysis

### 3.1 Solar-perturbed moon-to-moon transfer

In order to study the moon-to-moon transfer between the two gravity-assist manoeuvres, the circular restricted 3-body model is used, to account for the gravitational perturbation in the spacecraft's motion introduced by the non-negligible presence of the sun. It is to be noted that a planar assumption has been introduced: with the hypothesis that each body involved lies on the same plane  $X - Y$ , no force nor motion features a  $Z$  component.

To simplify the comparison among the various orbits and emphasize their differences, the transfer starting point is set at the intersection between the moon orbit and the  $x$  axis – in a non-rotating reference system centred on Earth –, corresponding to an angle  $\theta_{M_0} = 0^\circ$ . Moreover, the orbits are classified into two different categories: outbound-inbound, for the ones where the spacecraft's trajectory starts by moving away from Earth, and inbound-inbound, where, on the contrary, the spacecraft moves closer to Earth in the first phase of the manoeuvre.

The magnitude of the spacecraft's velocity vector relative to the moon is set at  $V_\infty = 1 \text{ km/s}$ , thus leading to a velocity relative to the inertial reference  $\mathbf{V}_{S/C} = \mathbf{V}_M + \mathbf{V}_\infty$ , where  $\mathbf{V}_M$  is the moon velocity vector relative to Earth. The angle  $\alpha$  between  $\mathbf{V}_\infty$  and  $\mathbf{V}_M$  is the first variable parameter, appear-

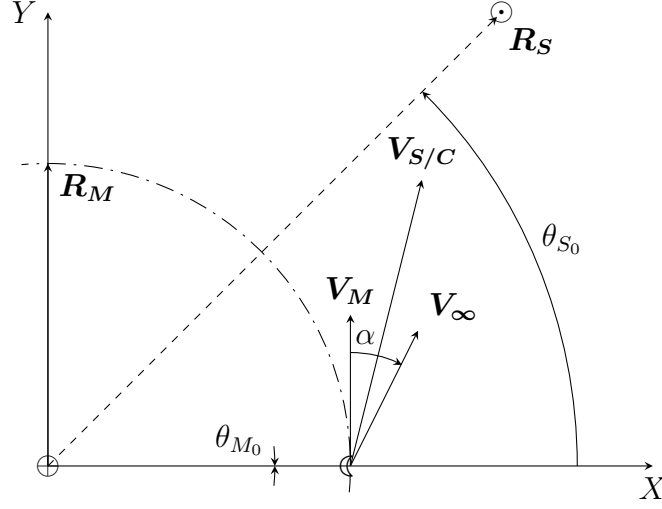


Figure 3.1: Geometrical schema for determination of moon-to-moon transfer orbits. Here the outbound-inbound example is shown, being  $\alpha > 0$ .

ing in the inner loop of the iteration process – varying from  $0^\circ$  to  $180^\circ$  for the outbound-inbound orbits and from  $-0.05^\circ$  to  $-179.95^\circ$  for the inbound-inbound, in  $0.05^\circ$  increments. The second varying parameter, defining the outer loop, is the initial position of the sun,  $\theta_{S_0}$ , which cycles from  $0^\circ$  to  $359^\circ$  in  $1^\circ$  increments. An explicative schema of the geometry of the problem is shown in figure 3.1.

The developed program integrates the equations of motion (2.32) from the following starting conditions:

$$\left\{ \begin{array}{l} X_0 = R_M \cos(\theta_{M_0}) \\ Y_0 = R_M \sin(\theta_{M_0}) \\ Z_0 = 0 \\ V_{X_0} = -V_M \sin(\theta_{M_0}) - V_\infty \sin(\theta_{M_0} - \alpha) \\ V_{Y_0} = V_M \cos(\theta_{M_0}) + V_\infty \cos(\theta_{M_0} - \alpha) \\ V_{Z_0} = 0 \end{array} \right. \quad (3.1)$$

The timespan of integration is set at 7 months, to avoid unreasonable flight times. However, integration is stopped earlier if an encounter with the lunar orbit is identified, and the moon's and spacecraft's angular positions are then

compared: if they are found to be relatively close to each other – less than  $10^\circ$  –, a subroutine is called, the task of which is to identify the exact value of  $\alpha$  that allows a spacecraft-moon re-encounter, achieving convergence via the secant method.

The sun gravitational perturbation has an almost exact  $180^\circ$  periodicity with respect to the position of the sun. Deviations have the same order of magnitude of  $\frac{r}{r_S}$ . For this reason, available moon-to-moon trajectories should exhibit the same periodicity.

The numerical search procedure described above may not converge and miss some solutions. To avoid this, a systematic search of solutions with sun's initial position translated by  $\pm 180^\circ$  is introduced.

$$\theta_{S_0, sym} = \theta_{S_0} + \pi \quad (3.2)$$

Then, the same approach as described above is followed. However, the search for  $\alpha_{sym}$  that are associated to a proper solution is restricted to the range  $\alpha$ , due to the aforementioned symmetry.

It can be observed, however, how many of the identified solutions are not meaningful in the context of this study: on the one hand, numerous duplicates appear, with the undesired effect of notably slowing down computation and bringing no benefit; on the other hand, some solutions do not bear a physical, reasonable meaning but only a mathematical one, due to an extremely limited orbit duration – even below 1 s. Thus, a filter is introduced to remove such false-positives.

Finally, solutions are grouped by family according to their orbit duration. Results are saved in a *.xlsx*, where each family is stored in a dedicated sheet, in the form of a  $N_i \times 13$  matrix – where  $N_i$  is the number of identified solutions for the  $i^{th}$  family. The matrix is assembled according to the following structure: columns from 1 to 6 consist of the coordinates of the spacecraft-moon rendezvous and the vector components of the spacecraft speed at the

encounter; column 7 is dedicated to the duration of the orbit (in  $s$ ); column 8 stores the value of  $\alpha$ , while column 9 stores the initial angular position of the Sun  $\theta_{S_0}$ ; columns 10 and 11 contain the angular position of both spacecraft and moon at the rendezvous (even though this means the same value is saved twice for each solution, this strategy has been adopted so as to have one more check regarding whether the rendezvous has been properly achieved), column 12 is dedicated to the conversion of  $T_E$  (from column 7) in lunar months; finally, column 13 stores the angular position of the Sun at the moment of rendezvous.

Once all the values of  $\alpha$  that allow for a moon-to-moon transfer are identified, the corresponding orbits are then drawn, after having classified them on the basis of their duration. Each family is assigned an unequivocal name, consisting of three letters: the first one, from A to F, identifies the family on the basis of the duration of the orbits, with A corresponding to  $T_E \simeq 1 \text{ month}$ , B to  $T_E \simeq 2 \text{ months}$ , and so on; the other two are used to distinguish whether the family includes outbound-inbound orbits or inbound-inbound ones. Thus, for example, a family consisting of outbound-inbound orbits that allow a rendezvous after circa 3 months is classified as *Coi*.

To account for the size of Earth and avoid both impacts and the possible dissipation of energy due to drag caused by the atmosphere (which would break the algorithm since there is no control over the conservation of mechanical energy), a minimum altitude of  $250 \text{ km}$  is enforced: in case during the integration process the magnitude of the spacecraft's distance vector from Earth's centre reaches  $R_{\oplus} + 250 \text{ km}$  or lower, integration is stopped and a warning is displayed.

## 3.2 Moon-to-escape lunar gravity assist

The evaluation of the LGA manoeuvre is performed starting from the results obtained during the moon-to-moon leg analysis. In particular, the spacecraft's position coordinates at the re-encounter, its velocity vector components, the value of  $\alpha$  (cf. section 3.1), the time of the encounter  $T_E$  (measured from the start of the integration process  $T_0$ ), the angular position of the spacecraft at the encounter, the angular position of the Sun both at  $T_0$  and at  $T_E$ , and the number of lunar revolutions between  $T_E$  and  $T_0$  are required. The periselene  $r_p$  is set at 50 km over the moon's surface, to avoid collisions during the manoeuvre.

### 3.2.1 Lunar gravity assist evaluation

To streamline the evaluation process and reduce the computing time, only one orbit family, selected at the moment of running the executable, is loaded. The evaluation proper follows, for every orbit in the selected family (outermost loop).

First, the velocity vector is converted from a Cartesian reference frame to a reference frame moving with the moon with the first axis along the Earth-moon direction, the second one perpendicular to the moon orbit plane, and the third one given by the right-hand rule, which means parallel to  $\mathbf{V}_M$ , thus yielding  $\mathbf{V}_\infty^-$ :

$$\begin{cases} u_\infty^- = V_{\infty,X} \cos \theta + V_{\infty,Y} \sin \theta \\ v_\infty^- = -V_{\infty,X} \sin \theta + V_{\infty,Y} \cos \theta - V_M \\ w_\infty^- = 0 \end{cases} \quad (3.3)$$

Where  $\theta$ , as explained in section 3.1, is the angular position shared by the spacecraft and the moon at the re-encounter.

It is to be noted that the normal component of  $\mathbf{V}_\infty^-$  is null since the moon-to-moon leg lies on the moon orbit plane.

The pump angle at the start of the LGA manoeuvre can then be calculated from the radial and tangential components of  $\mathbf{V}_\infty^-$ , since:

$$p^- = \arctan \frac{u_\infty^-}{v_\infty^-} \quad (3.4)$$

After calculating  $p^-$ , the maximum possible rotation that can be induced by the LGA  $\delta_{max}$  is evaluated:

$$\delta_{max} = 2 \arcsin \frac{\mu_M/r_p}{V_\infty^{-2} + \mu_M/r_p} \quad (3.5)$$

Thus, an inner loop starts in which the possible pump angles after the LGA are considered:

$$p^- - \delta_{max} < p^+ < p^- + \delta_{max} \quad (3.6)$$

Since:

$$0 < \delta < \delta_{max} \quad (3.7)$$

For each  $p^+$ , all possible crank angles after the LGA are considered, from 0 to the maximum value  $k_{max}^+$ , in the innermost loop, where  $k_{max}^+$  can be calculated from the definition of dot product:

$$\mathbf{V}_\infty^- \cdot \mathbf{V}_\infty^+ = V_\infty^2 \cos \delta \quad (3.8)$$

Expressing the dot product using pump and crank angles (eq. 2.39), and noting that  $k^- = 0$ :

$$\cos \delta = \cos p^- \cos p^+ + \sin p^- \sin p^+ \cos k^+ \quad (3.9)$$

It is now possible to isolate  $\cos k^+$  from equation 3.9:

$$\cos k^+ = \frac{\cos \delta - \cos p^- \cos p^+}{\sin p^- \sin p^+} \quad (3.10)$$

Thus:

$$k_{max}^+ = \arccos \left( \frac{\cos \delta_{max} - \cos p^- \cos p^+}{\sin p^- \sin p^+} \right) \quad (3.11)$$

Remembering the limits for  $\delta$  mentioned in equation 3.7, it can be inferred that:

$$\cos \delta > \cos \delta_{max} \quad (3.12)$$

Thus, from equation 3.9:

$$\sin p^- \sin p^+ \cos k^+ > \cos \delta_{max} - \cos p^- \cos p^+ \quad (3.13)$$

Let us call  $arg$  the argument of the arccosine function in equation 3.11:

$$arg = \frac{\cos \delta_{max} - \cos p^- \cos p^+}{\sin p^- \sin p^+} \quad (3.14)$$

To ensure  $k_{max}^+$  is properly computed, a check is performed considering both the value  $arg$  and the sign of its denominator. It is to be noted that, for  $k^+ = 0$  in equation 3.9:

$$\cos \delta = \cos p^- \cos p^+ + \sin p^- \sin p^+ = \cos |\Delta p| > \cos \delta_{max} \quad (3.15)$$

Consequently:

$$\begin{aligned} \sin p^- \sin p^+ > 0 &\longrightarrow arg < 1 \\ \sin p^- \sin p^+ < 0 &\longrightarrow arg > 1 \end{aligned} \quad (3.16)$$

There are only three possible alternatives, as the others do not yield meaningful solutions – or any at all:

- $\sin p^- \sin p^+ > 0$ ,  $-1 < arg < 1 \longrightarrow k_{max}$  is computed according to equation 3.11;
- $\sin p^- \sin p^+ > 0$ ,  $arg < -1 \longrightarrow k_{max} = 180^\circ$ ;
- $\sin p^- \sin p^+ < 0$  (i.e. the gravity assist manoeuvre changes the sign of the pump angle)  $\longrightarrow k_{max} = 180^\circ$ .

Inside the innermost loop, the velocity relative to the moon after the LGA manoeuvre is evaluated for every  $k^+$ , exploiting once more equations 2.39.

Then, the absolute velocity in Earth's reference frame is obtained:

$$\begin{cases} u^+ = u_\infty^+ \\ v^+ = v_\infty^+ + V_M \\ w^+ = w_\infty^+ \end{cases} \quad (3.17)$$

To identify the value of the escape velocity, it is first necessary to calculate the energy associated to the orbit the spacecraft now lies upon.

$$\mathcal{E} = \frac{V^{+2}}{2} - \frac{\mu_E}{R_M} \quad (3.18)$$

Since the analysis is focused on evasion manoeuvres, the algorithm stops here and moves to the next iteration if the energy  $\mathcal{E}$  is negative, i.e. associated to a closed orbit.

Thus, the characteristic energy can be obtained:

$$C3 = 2\mathcal{E} \quad (3.19)$$

Assuming  $r \rightarrow \infty$  at the escape, the magnitude of the escape velocity vector follows:

$$V_{esc} = \sqrt{C3} \quad (3.20)$$

Other defining values characterizing the spacecraft's orbit can be inferred as well. First is the specific angular momentum:

$$h = R_M \sqrt{v^{+2} + w^{+2}} \quad (3.21)$$

It can be then exploited to obtain the value of the orbit eccentricity (expected to be greater than 1, since  $\mathcal{E} > 0$ ):

$$e = \sqrt{1 + \frac{2\mathcal{E}h^2}{\mu_E^2}} \quad (3.22)$$

From the expression of  $\mathcal{E}$  dependent on the orbit size, follows the evaluation of the semi-major axis:

$$a = -\frac{\mu_E}{2\mathcal{E}} \quad (3.23)$$

Consequently, the semilatus rectum can be calculated as:

$$p = a(1 - e^2) \quad (3.24)$$

Similarly, the perigee can be computed as well:

$$r_p = a(1 - e) \quad (3.25)$$

Then, the true anomaly can be isolated in equation 2.30:

$$\nu = \arccos \frac{p/R_M - 1}{e} \quad (3.26)$$

The true anomaly identifies the position of the spacecraft on its hyperbolic orbit, its aperture being identified by:

$$\varphi = \arccos \frac{1}{e} \quad (3.27)$$

Another check is then performed, to ensure collisions with Earth are avoided: if the true anomaly,  $\nu$ , is negative (i.e. the spacecraft is approaching the perigee), the perigee obtained from equation 3.25 is compared to Earth's radius increased by 200 km: in case  $r_p$  is found to be inferior to said value, the code skips to the next iteration and ignores the present solution.

It is now possible to evaluate the angle between the direction corresponding to the true anomaly after the LGA and the direction of  $\mathbf{V}_{esc}$  (figure 3.2):

$$\Delta = \pi - \varphi - \nu \quad (3.28)$$

The inclination of the escape orbit can also be inferred from  $\mathbf{V}^+$  components:

$$i = \arctan \frac{w^+}{v^+} \quad (3.29)$$

It is now necessary to consider the angular position of the LGA relative to the sun's, by introducing angle  $\Omega$ :

$$\Omega = \theta - \theta_S \quad (3.30)$$

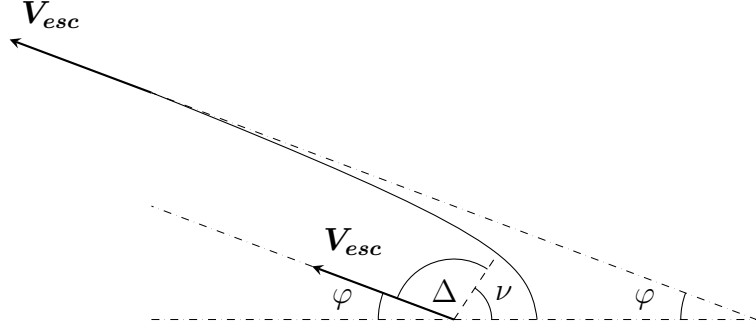


Figure 3.2: Geometrical schema for escape orbit.

Finally, it is possible to determine the components of the spacecraft's velocity  $\mathbf{V}_H$  in a radial-tangential-normal reference system centred at the sun, considering the effects of  $\Delta$ ,  $i$ , and  $\Omega$  on the reference change:

$$\begin{cases} \frac{u_H}{V_H} = \sin \Delta \sin \Omega \cos i - \cos \Delta \cos \Omega \\ \frac{v_H}{V_H} = -\sin \Delta \cos \Omega \cos i - \cos \Delta \sin \Omega \\ \frac{w_H}{V_H} = \sin \Delta \sin i \end{cases} \quad (3.31)$$

Note that  $V_{esc} = V_H$ , since it is the same vector expressed in two different reference frames.

Thus, as shown in figure 3.3, the heliocentric flight-path angle ( $\gamma_H$ ) and declination ( $\delta_H$ ) for the spacecraft's velocity after the LGA manoeuvre are evaluated:

$$\begin{cases} \gamma_H = \arctan \frac{u_H}{v_H} \\ \delta_H = \left| \arcsin \frac{w_H}{V_H} \right| \end{cases} \quad (3.32)$$

In equation 3.32,  $\delta_H$  is computed using the modulus since the manoeuvre is symmetrical: since it is sufficient to invert  $k^+$  to change the sign of  $\delta_H$ , it is possible to limit the study to positive values for declination.

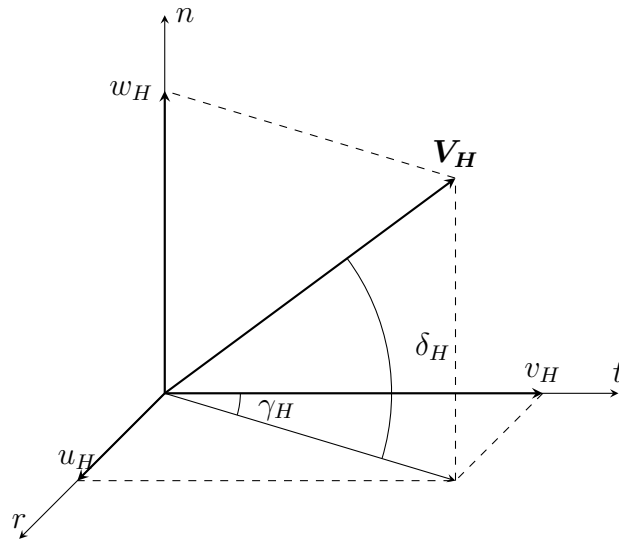


Figure 3.3: Heliocentric flight-path angle ( $\gamma_H$ ) and declination ( $\delta_H$ ) for the spacecraft's velocity after the lunar gravity assist.

### 3.2.2 Maximum $C3$ , given heliocentric flight-path angle and declination

The procedure for evaluating the effect of the lunar gravity assist manoeuvre, described in section 3.2.1, allows to obtain three matrices as output for each of the solutions found for the moon-to-moon leg, each one associating a value for  $C3$ ,  $\gamma$ , and  $\delta^1$  respectively, to a couple  $(p^+, k^+)$ .

The goal of the study, however, is to directly link  $C3$  to  $\gamma_H$  and  $\delta_H$ . Thus, the final part of the algorithm was developed to interpolate data coming from the three aforementioned matrices.

For each couple  $(p^+, k^+)$  considered during the LGA evaluation, the corresponding values for  $C3$ ,  $\gamma$ , and  $\delta$  are taken from the respective matrix, and the last two are rounded to the nearest integer. Consequently, it can be written that:

<sup>1</sup>From here onwards, the subscript  $H$  for  $\gamma$  and  $\delta$  will be omitted for simplicity.

$$\begin{aligned}\gamma &\longrightarrow 0 \leq g \leq 359, \quad g \in \mathbb{N} \\ \delta &\longrightarrow 0 \leq d \leq 90, \quad d \in \mathbb{N}\end{aligned}\tag{3.33}$$

Therefore,  $(g + 1)$  and  $(d + 1)$  can be used as indices to fill a matrix with the value of  $C3$  related to the  $\gamma$  and  $\delta$  from which  $g$  and  $d$  have been taken. In case the couple  $(g, d)$  repeats itself, the higher  $C3$  is saved, while the lower one is discarded.

Thus, a matrix  $C3_{max}(g, d) \in \mathbb{R}^{360 \times 91}$  is created for each family, where the maximum achievable value of  $C3$  given  $\gamma$  and  $\delta$  is stored.

Finally, the twelve matrices that have been obtained need to be assembled for a global evaluation. For each  $(g, d)$  couple, the values of  $C3$  from each of the twelve families are compared and the maximum one among them is saved in a dedicated matrix, resulting in a map that associates to a given  $\gamma$  and a given  $\delta$  the maximum achievable energy value for the resulting orbit after the lunar gravity assist manoeuvre, independently from the duration of the moon-to-moon leg.

# Chapter 4

## Results

### 4.1 Moon-to-moon leg

In this section, the orbits allowing a rendezvous between the spacecraft and the moon are shown, for both outbound-inbound and inbound-inbound families.

#### 4.1.1 Outbound-inbound

As far as outbound-inbound families are concerned (figure 4.1), it is evident how trajectories that allow a rendezvous between the spacecraft and the moon are possible for a limited range of  $\alpha$ . This range has been found to be dependent upon the family (i.e. the duration of the moon-to-moon leg): while for *Aoi* family the interval in which solutions have been found is limited to  $\sim 4^\circ$  ( $110.50^\circ - 114.75^\circ$ ), *Foi* family shows a fivefold variation range ( $87.81^\circ - 108.52^\circ$ ). The longer the orbit, the wider the possible range of  $\alpha$  where a solution can be identified is. It is to be noted, though, how the upper boundary of said range does not show an important variation, since it stays close to  $110^\circ$  for each family. On the other hand, the lower end of the range decreases steadily with the increase of  $T_E$ , meaning that the first LGA manoeuvre can have more outcomes that result viable for a moon-to-moon trajectory.

Table 4.1: Ranges (in  $^\circ$ ) for  $\alpha$  and  $\theta_{SC}$  for oi families.

Family	$\alpha_{min}$	$\alpha_{max}$	$\alpha$ range	$\theta_{SC,min}$	$\theta_{SC,max}$	$\theta_{SC}$ range
<i>Aoi</i>	110.50	114.75	4.25	66.98	113.97	46.99
<i>Boi</i>	101.40	109.93	8.53	50.27	179.87	129.60
<i>Coi</i>	96.22	109.63	13.41	10.05	247.69	237.64
<i>Doi</i>	92.59	108.86	16.27	-31.63	284.63	316.25
<i>Eoi</i>	89.92	108.81	18.89	1.96	359.68	357.72
<i>Foi</i>	87.81	108.52	20.71	0.34	359.69	359.35

Furthermore, another consideration worth noticing concerns the location of the rendezvous  $\theta_{SC}$ : with longer time available and a wider range of  $\alpha$ , the last families allow re-encounters almost all along moon's orbit, which is not true for *Aoi*, *Boi*, and *Coi*.

Finally, the disturbing effect of the Sun on the spacecraft orbit can be highlighted: long-lasting orbits that achieve relevant distances from Earth show notable irregularities that are not compatible with a Newtonian description of the orbital motion, while shorter legs appear to be more regular and devoid of inversions – even though the orbits are not simply conic any more in these cases as well.

### 4.1.2 Inbound-inbound

Inbound-inbound orbits, shown in figure 4.2, are subject to similar considerations to the ones applicable to oi families.

The range of  $\alpha$  once again increases with the duration of the orbit, in a similar fashion to what has been seen for oi families. The upper and lower boundaries switch their role, meaning that for inbound-inbound orbits the lower end is the one showing the less amount of variation (from  $-120.65^\circ$  for *Aii* to  $-108.58^\circ$  for *Fii*) compared to the higher end (from  $-117.84^\circ$  to  $-87.86^\circ$ ). This role inversion, however, is logical and expected: as shown by

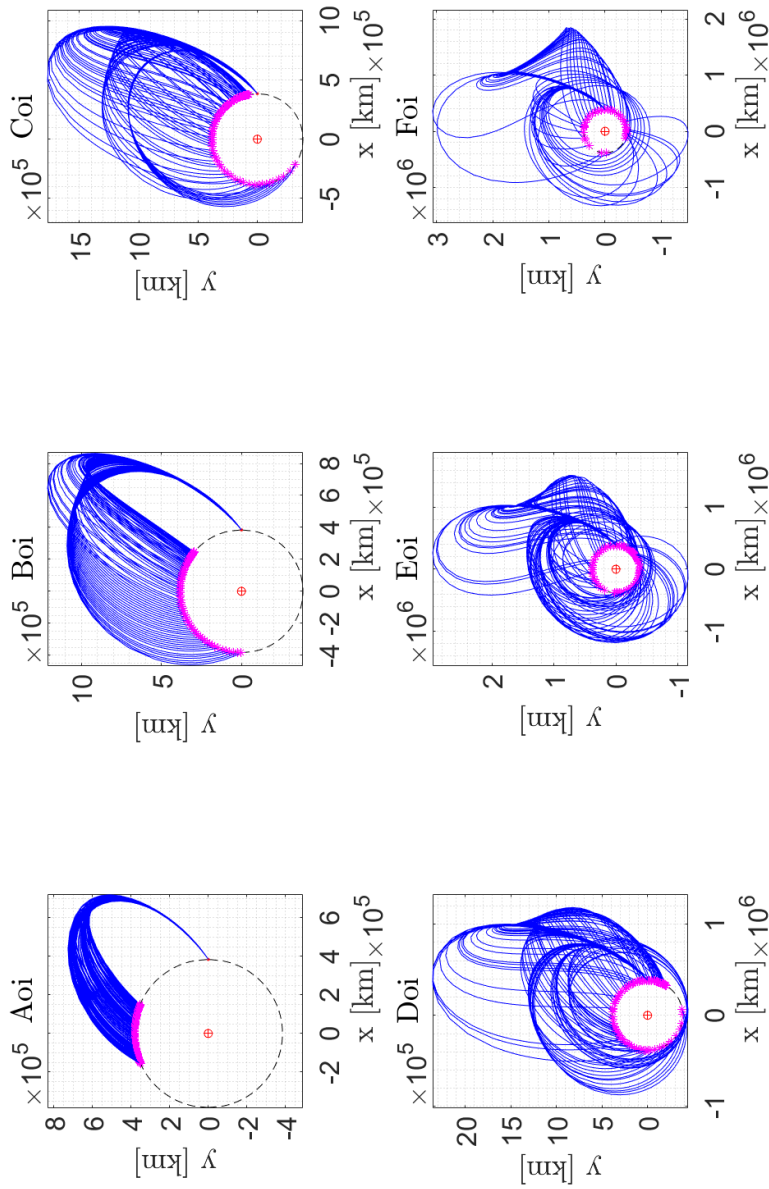


Figure 4.1: Outbound-inbound orbits. Initial and final positions of the moon are shown by red circles and magenta asterisks, respectively. The dashed circumference shows the lunar orbit around Earth, assumed circular.

Table 4.2: Ranges (in  $^\circ$ ) for  $\alpha$  and  $\theta_{SC}$  for ii families.

Family	$\alpha_{min}$	$\alpha_{max}$	$\alpha$ range	$\theta_{SC,min}$	$\theta_{SC,max}$	$\theta_{SC}$ range
<i>Aii</i>	-120.65	-117.84	2.80	-7.37	9.33	16.7
<i>Bii</i>	-111.40	-104.94	6.46	-35.30	95.68	130.98
<i>Cii</i>	-109.25	-98.82	10.43	-92.34	167.02	259.36
<i>Dii</i>	-108.75	-93.00	15.75	3.84	335.74	331.90
<i>Eii</i>	-108.62	-90.00	18.62	-17.42	328.88	346.30
<i>Fii</i>	-108.58	-87.86	20.72	2.06	355.68	353.63

oi families, longer-lasting orbits allow values of  $\alpha$  determining a  $\mathbf{V}_\infty$  closer to  $\mathbf{V}_M$ , compared to shorter ones.

The phenomenon of the rendezvous location moving from a small interval for the first families to the almost complete moon orbit is here even more accentuated. *Aii* shows a  $\theta_{SC}$  at the re-encounter varying in a limited  $\sim 17^\circ$  interval around  $0^\circ$ , even smaller than the  $\sim 47^\circ$  range for *Aoi*.

Finally, the perturbation originating from the gravitational effect caused by the Sun is once again extremely clear for the last families, where the same irregularities and inversions identified for oi families appear.

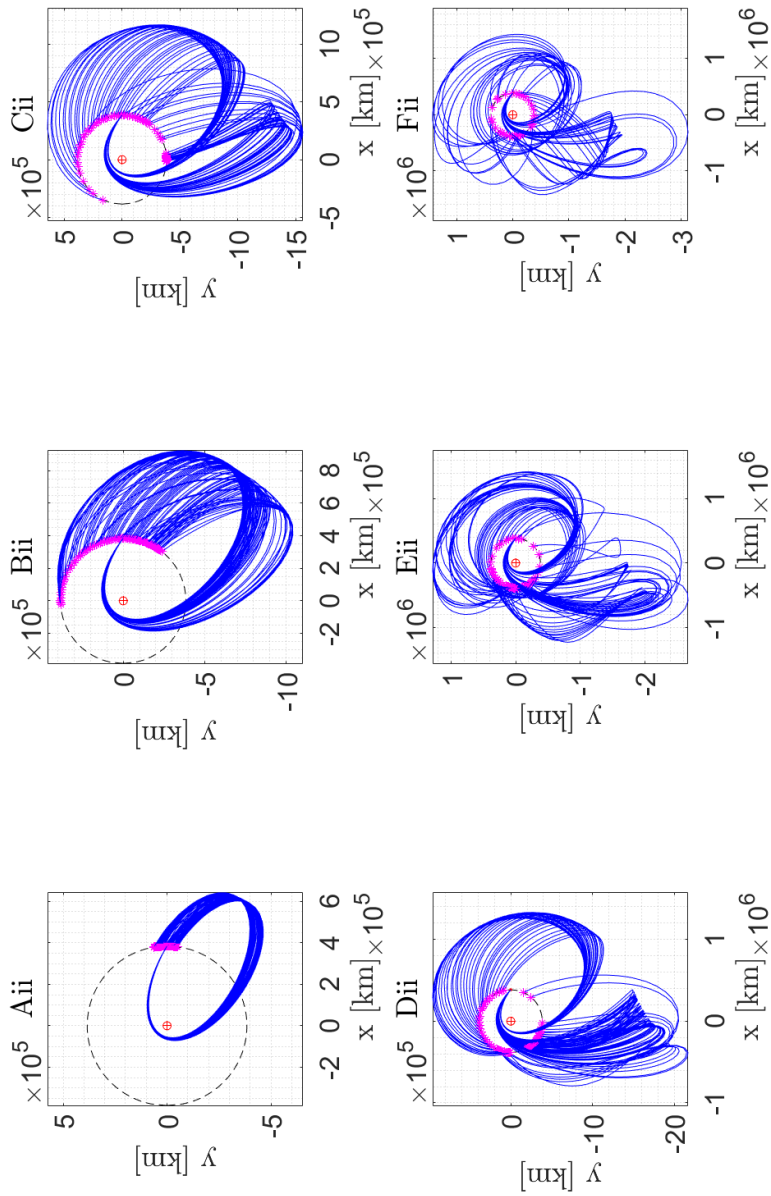


Figure 4.2: Inbound-inbound orbits. Initial and final positions of the moon are shown by red circles and magenta asterisks, respectively. The dashed circumference shows the lunar orbit around Earth, assumed circular.

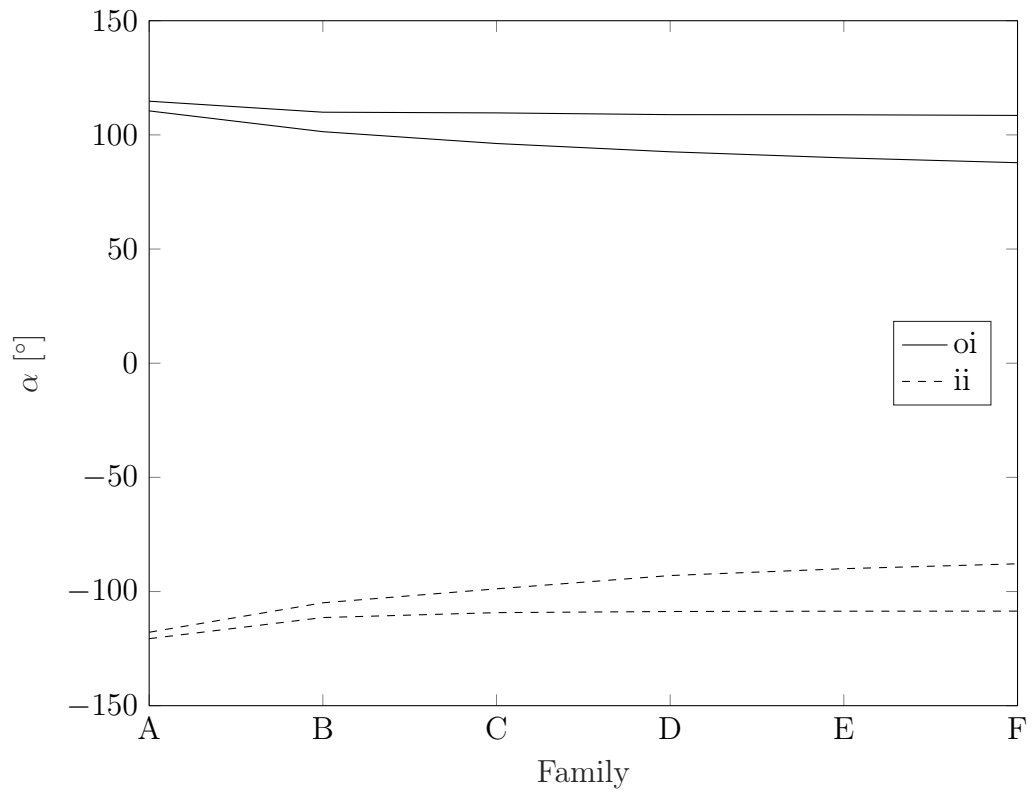


Figure 4.3: Range of  $\alpha$  that allow a rendezvous for oi and ii families.

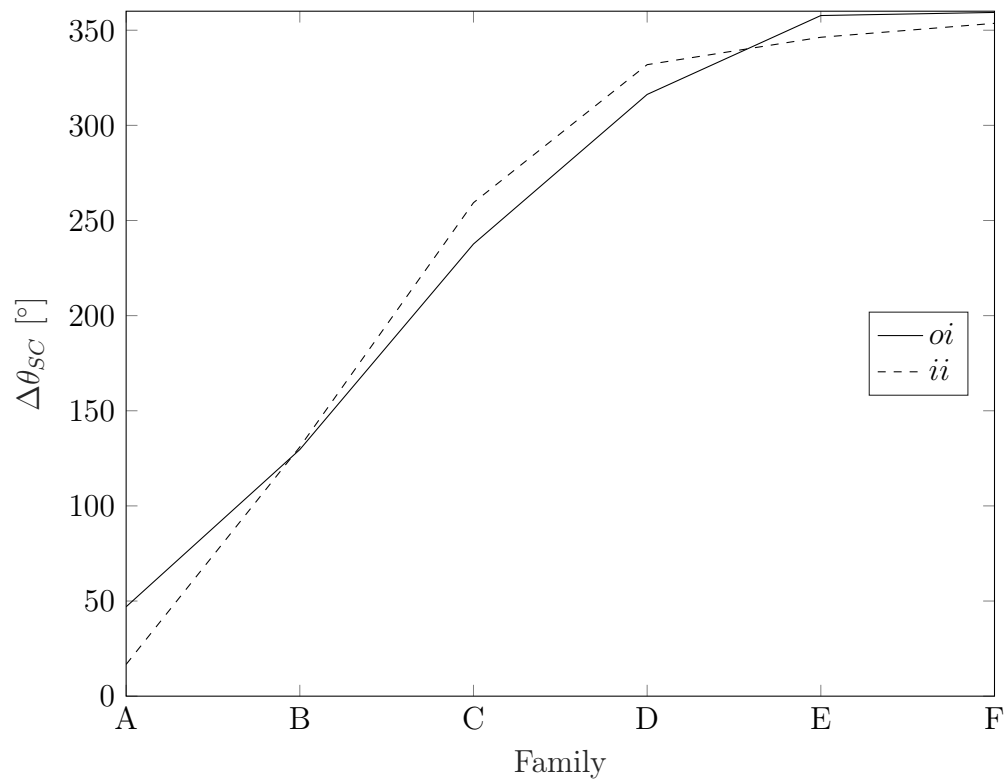


Figure 4.4: Range of  $\theta$  that allow a rendezvous for oi and ii families.

## 4.2 Lunar gravity assist

In this section, the maps linking the maximum  $C3$  achievable to both flight-path angle and declination of the spacecraft velocity at the escape are shown, together with graphs where  $C3(\gamma)$  is compared for different values of  $\delta$ .

### 4.2.1 $C3(\gamma, \delta)$ maps

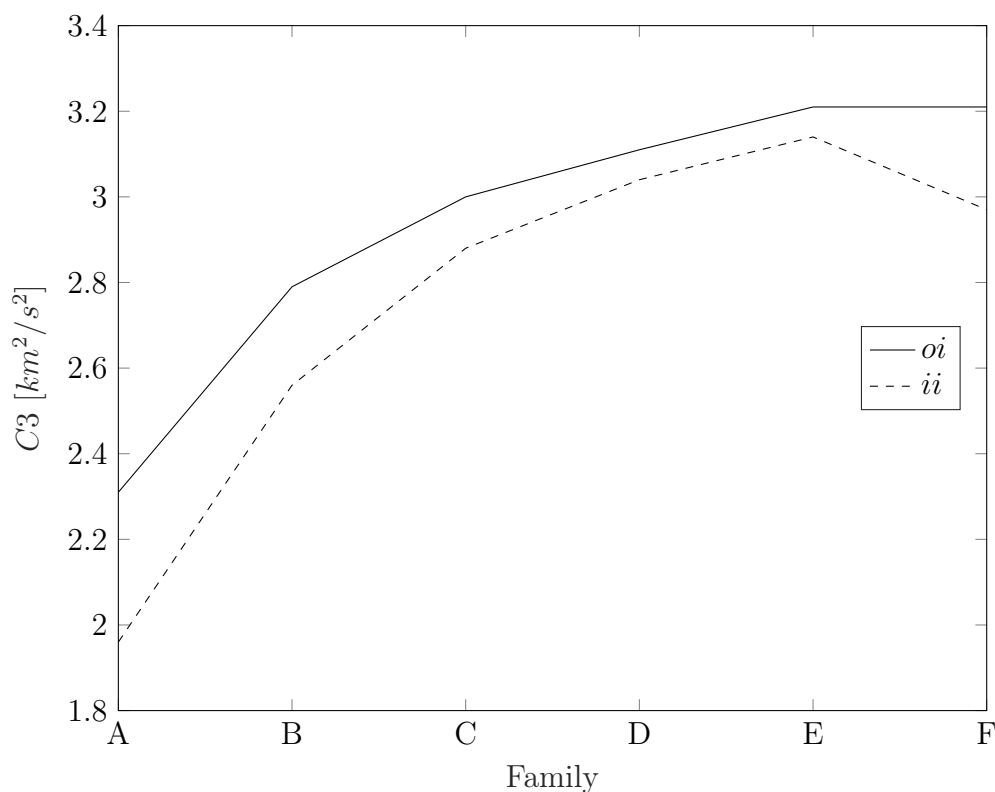
As far as maps are concerned, they have been created from the matrices mentioned in section 3.2.2. Heliocentric flight-path angle is on the x-axis, while declination is on the y-axis. The values of  $C3$  are represented using a colour scale:

- $0 \leq C3 \leq 1 \text{ km}^2/\text{s}^2$   $\longrightarrow$  colour varies linearly from white to magenta;
- $1 < C3 \leq 2 \text{ km}^2/\text{s}^2$   $\longrightarrow$  colour varies linearly from magenta to blue;
- $2 < C3 \leq 3 \text{ km}^2/\text{s}^2$   $\longrightarrow$  colour varies linearly from blue to green;
- $3 < C3 \leq 4 \text{ km}^2/\text{s}^2$   $\longrightarrow$  colour varies linearly from green to yellow;
- $4 < C3 \leq 5 \text{ km}^2/\text{s}^2$   $\longrightarrow$  colour varies linearly from yellow to red.

Figures from 4.6 to 4.17 show the results of the interpolation of  $C3$  described in section 3.2.2. All maps share a periodicity around  $180^\circ$ , due to the nature of the perturbation effect generated by the Sun (see section 3.1). Thus, considerations can be limited to  $\gamma \in [0^\circ, 180^\circ]$ . Moreover, it can be observed how higher values for characteristic energy ( $C3$ ) are generally confined to reduced declinations, regardless of family - even though values themselves tend to change and increase with longer-lasting orbits.

Table 4.3: Maximum  $C3$  [ $km^2/s^2$ ] achievable for each family.

Family	<i>A</i>	<i>B</i>	<i>C</i>	<i>D</i>	<i>E</i>	<i>F</i>
<i>oi</i>	2.31	2.79	3.00	3.11	3.21	3.21
<i>ii</i>	1.96	2.56	2.88	3.04	3.14	2.97

Figure 4.5: Maximum  $C3$  achievable for each family.Table 4.4: Minimum guaranteed  $C3$  [ $km^2/s^2$ ] achievable for each family.

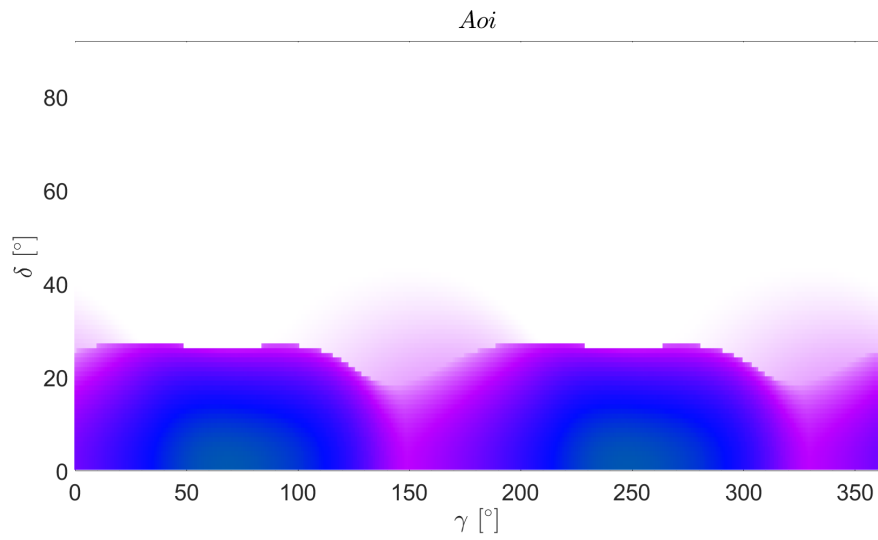
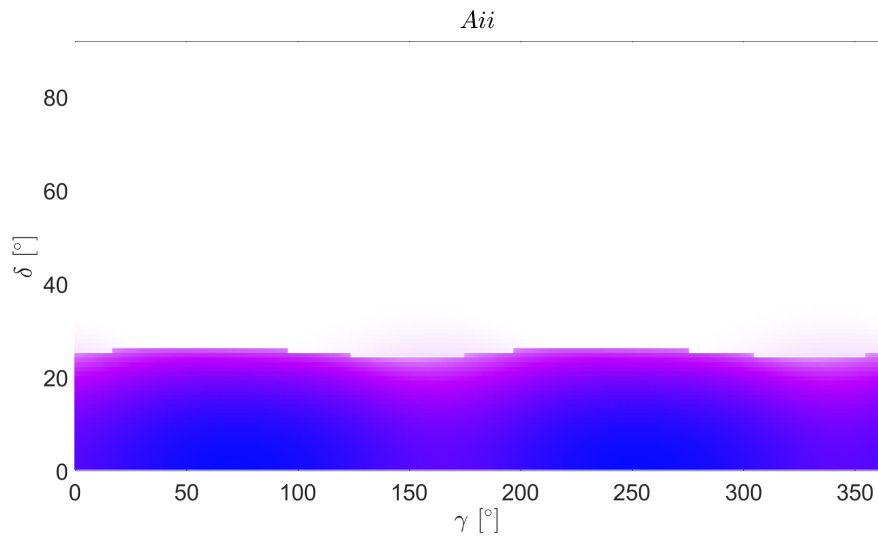
Where 0 is listed, it means that not every couple  $(\gamma, \delta)$  is achievable.

Family	<i>A</i>	<i>B</i>	<i>C</i>	<i>D</i>	<i>E</i>	<i>F</i>
<i>oi</i>	0	0	0.40	1.45	0	0
<i>ii</i>	0	0	0	1.02	1.22	0

*Aoi – Aii*

For *Aoi* family, the maximum achievable  $C3$  is  $C3 \simeq 2.31 \text{ km}^2/\text{s}^2$  – thus  $V_{esc} \simeq 1.52 \text{ km/s}$  – for a flight-path angle close to  $70^\circ$ .  $C3 > 2 \text{ km}^2/\text{s}^2$  can only be achieved for declination lower than  $15^\circ$ , while  $\gamma$  must fall within  $40^\circ$  and  $110^\circ$ . Almost no escape with a moon-to-moon leg belonging to *Aoi* family is possible for  $\delta > 30^\circ$ . *Aii* is similar, but shows lower values for  $C3$ : as a matter of fact, it does not even reach  $2 \text{ km}^2/\text{s}^2$ , peaking at  $C3 = 1.96 \text{ km}^2/\text{s}^2$  –  $V_{esc} = 1.4 \text{ km/s}$ .

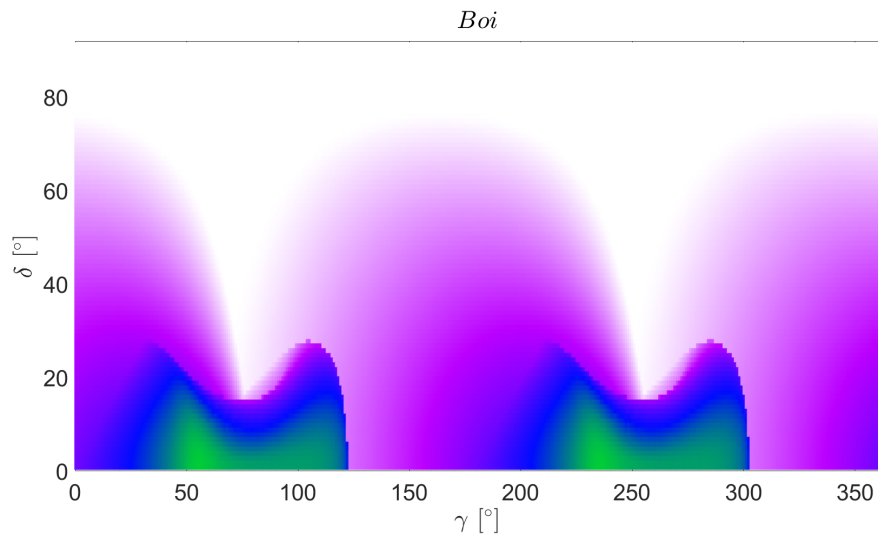
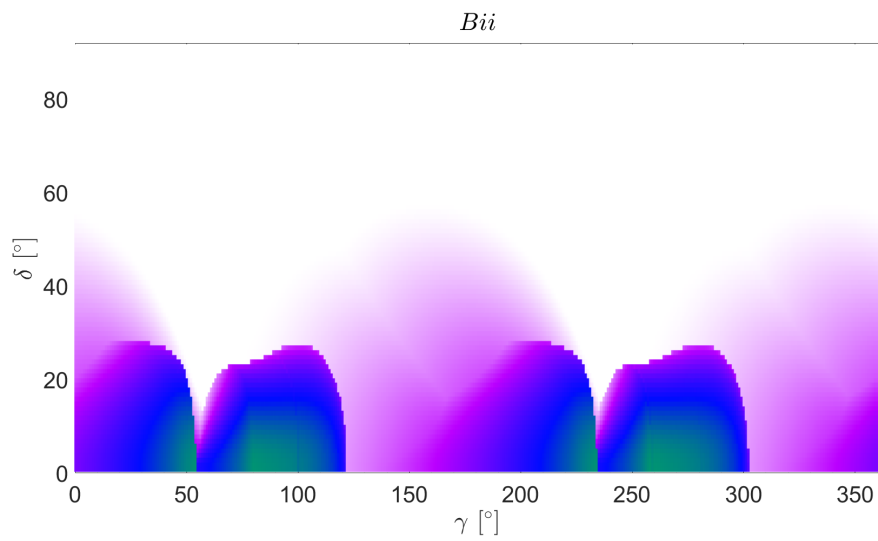
Finally, both maps, as well as the ones presented hereinafter, highlight the aforementioned 180-degree periodicity.

Figure 4.6:  $C3(\gamma, \delta)$  map for *Aoi* family.Figure 4.7:  $C3(\gamma, \delta)$  map for *Aii* family.

*Boi – Bii*

*Boi* family allows the achievement of higher characteristic energies, up to  $2.79 \text{ km}^2/\text{s}^2 - V_{esc} \simeq 1.67 \text{ km/s}$ , compared to *Aoi*. Once again, higher values can be found for low declination, however, two peaks can be identified instead of a single one: a first, more prominent one for  $\gamma \simeq 50^\circ$ ; then, a second, shorter one just after  $\gamma \simeq 100^\circ$ . From the comparison between figures 4.6 and 4.8 it can be inferred how longer transfers between the two gravity assist manoeuvres allow for more energetic escapes and can be exploited to obtain higher declination for  $V_{esc}$  over the ecliptic plane.

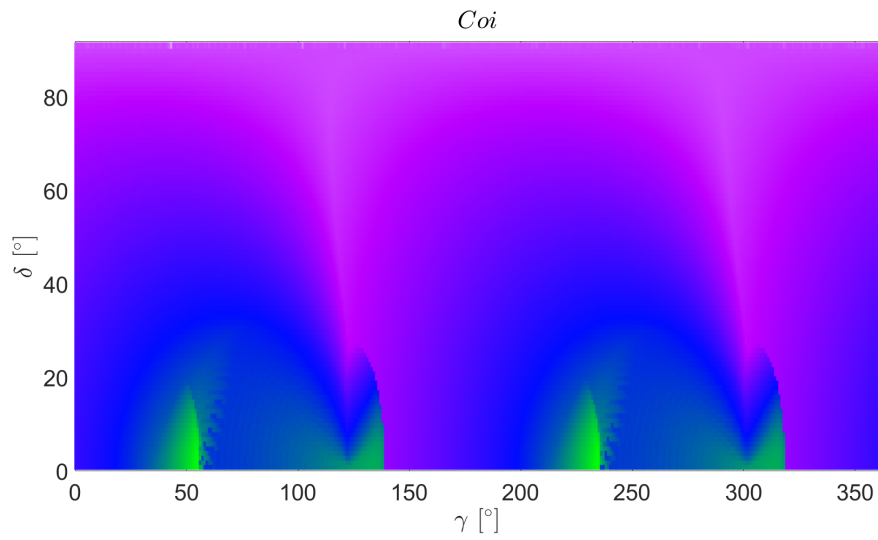
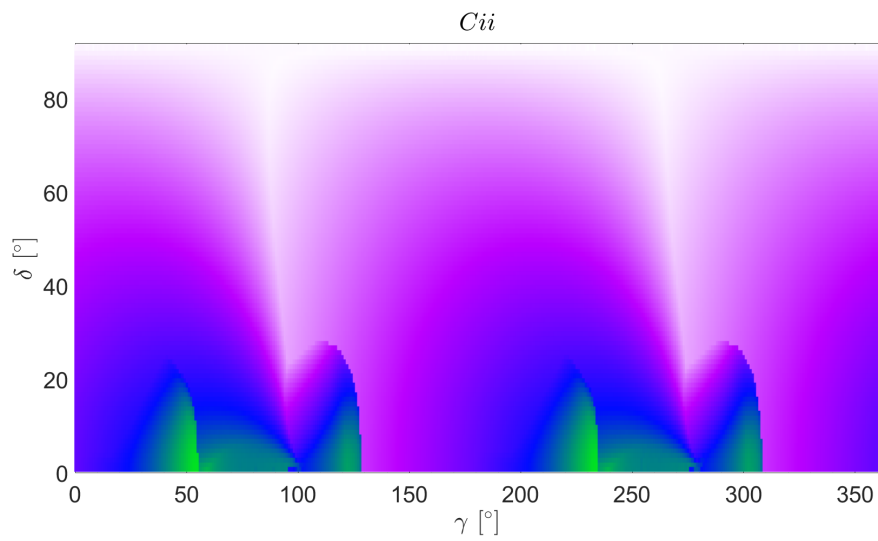
Similarly, *Bii* shows two peaks as well. The same phenomenon that has been highlighted for oi families is evident: here  $C3 \leq 2.56 \text{ km}^2/\text{s}^2$ .

Figure 4.8:  $C3(\gamma, \delta)$  map for *Boi* family.Figure 4.9:  $C3(\gamma, \delta)$  map for *Bii* family.

*Coi – Cii*

Accepting transfers of approximately 3 months or longer is necessary if escapes with high declination for any  $\gamma$  are desired. As mentioned above, characteristic energy is higher than what is achievable with shorter moon-to-moon legs, and inbound-inbound orbits appear to allow less energetic escapes compared to their outbound-inbound counterpart:  $C3 = 2.88 \text{ km}^2/\text{s}^2$  versus  $C3 = 3.00 \text{ km}^2/\text{s}^2$ .

Similarly to *B* families, *C* families show multiple peaks as well, instead of a single one.

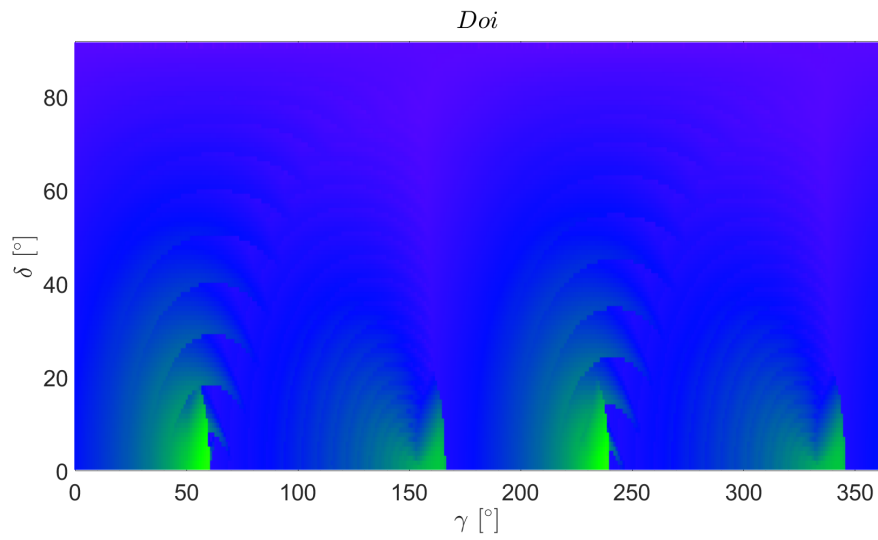
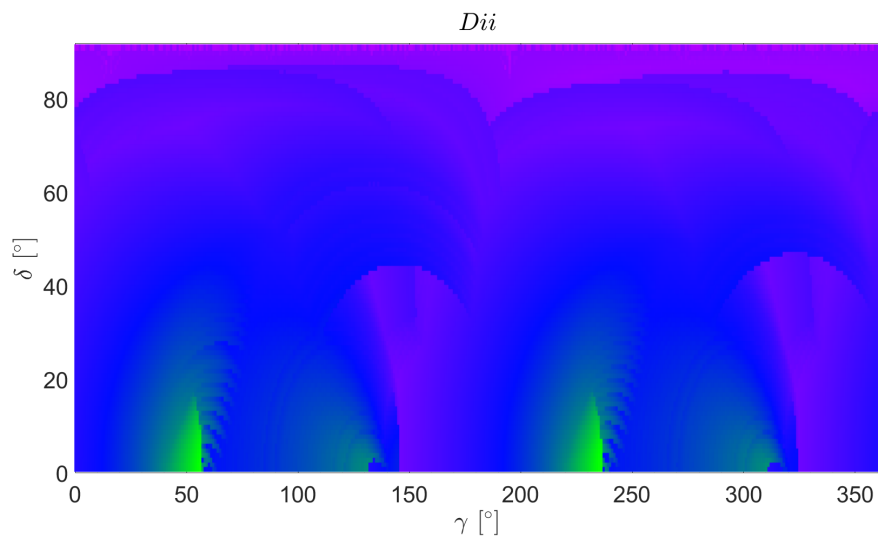
Figure 4.10:  $C3(\gamma, \delta)$  map for *Coi* family.Figure 4.11:  $C3(\gamma, \delta)$  map for *Cii* family.

*Doi – Dii*

It can be noted how moon-to-moon legs belonging to *D* family or higher, as far as both outbound-inbound and inbound-inbound orbits are concerned, ensure that any escape can be achieved with  $C3 \geq 1 \text{ km}^2/\text{s}^2$ , thus velocities at the escape  $V_{esc} \geq 1 \text{ km/s}$ .

However, a criticality faced during the study emerges from *D* family onwards: the maps (and also, consequently, the graphs shown in the following section) start to feature notable irregularities, that increase in relevance with last families. It is also evident from table 4.4, since it appears that *Eoi*, *Foi*, and *Fii* families do not allow some  $(\gamma, \delta)$  couples at the escape.

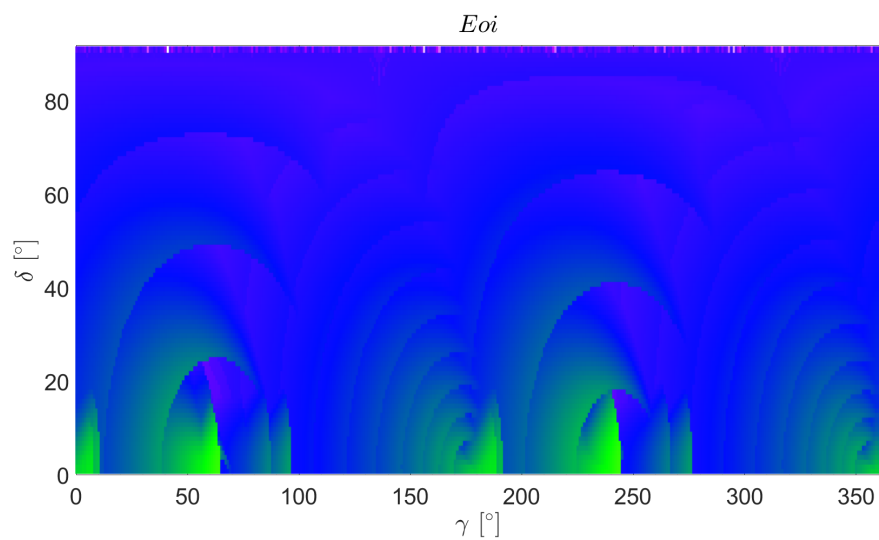
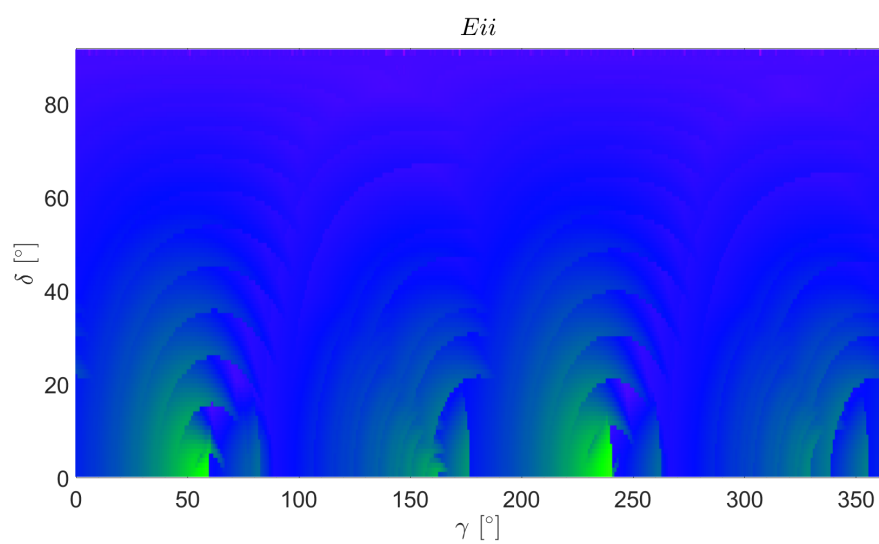
It has been hypothesised that such discrepancies from the expected, more regular behaviour are caused by unidentified solutions leading to a lunar gravity assist. Thus, as it will be mentioned in the conclusive chapter, one of the possibilities for the development of this study and topic of future research activity should be focused on identifying such missed rendezvous. Moreover, the hyperbolic excess velocity at re-encounter of the moon is quite large for these families. Even small differences may remarkably alter the escape outcome and a more detailed exploration of the solutions should be performed.

Figure 4.12:  $C3(\gamma, \delta)$  map for *Doi* family.Figure 4.13:  $C3(\gamma, \delta)$  map for *Di* family.

*Eoi – Eii*

Similar considerations to the ones for earlier families apply to *E* family: peak *C3* increases and is higher for outbound-inbound orbits compared to their counterpart. Yet, both the increase from previous families and the difference between oi and ii are less evident, and ii orbits appear to be more and more similar to oi, in terms of escape conditions.

Moreover, it can be noted how the minimum value for *C3* appears to be  $0 \text{ km}^2/\text{s}^2$ , meaning that not all escape conditions in terms of  $\gamma$  and  $\delta$  are possible, which contrasts with the previous finding that later families are associated with higher *C3* for any given  $(\gamma, \delta)$ . However, this irregularity is associated to declination close to  $90^\circ$ , where multiple inconsistencies appear and, thus, the obtained results are not reliable.

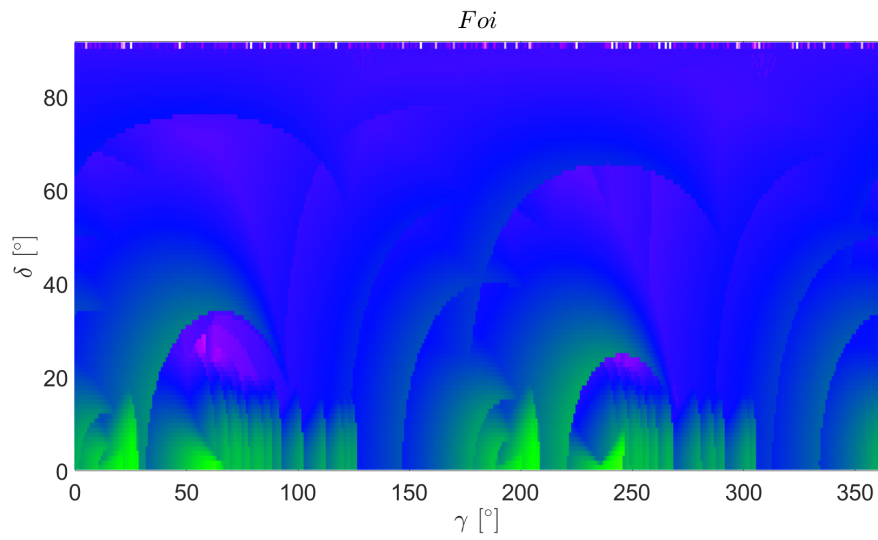
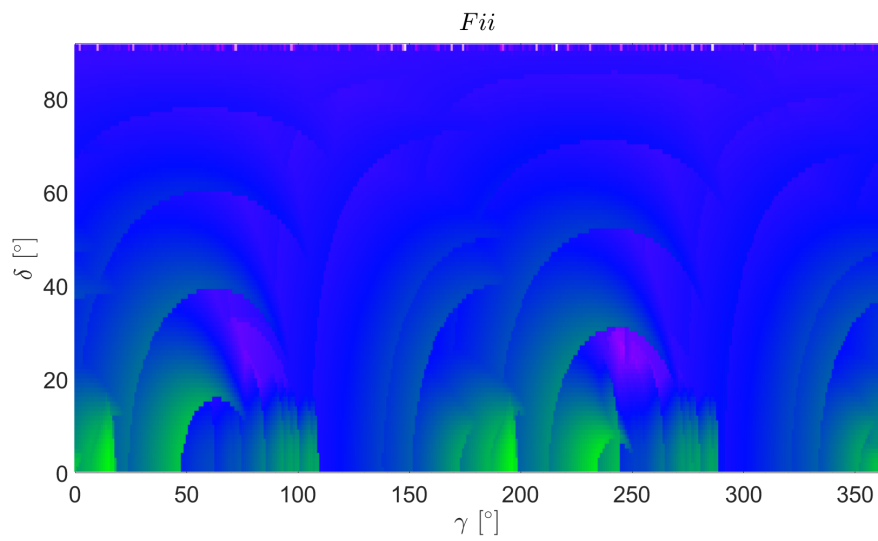
Figure 4.14:  $C3(\gamma, \delta)$  map for *Eoi* family.Figure 4.15:  $C3(\gamma, \delta)$  map for *Eii* family.

*Foi – Fii*

*F* families distinguish themselves from the previous ones due to some peculiar features, that suggest possible paths for future research.

First, both outbound-inbound and inbound-inbound show a minimum  $C3 = 0 \text{ km}^2/\text{s}^2$ , again meaning that not all escape conditions in terms of  $\gamma$  and  $\delta$  are possible. This issue, however, is likely to have its roots in the same irregularities that stemmed this very problem for *E* families.

Furthermore, *F* families seem to invert the trend related to the increase of the peak  $C3$  and the parallel reduction of the gap between oi and ii. As shown in figure 4.5, maximum characteristic energy for *Foi* is the same as that for *Eoi*, and for inbound-inbound orbits it even decreases – from  $3.14 \text{ km}^2/\text{s}^2$  to  $2.97 \text{ km}^2/\text{s}^2$ . It might be worth focusing future research on this apparent inversion, to understand whether *E* families are the ones that allow more energetic escapes or, alternatively, the computational inaccuracy witnessed for the last families is to be blamed for this trend change.

Figure 4.16:  $C3(\gamma, \delta)$  map for *Foi* family.Figure 4.17:  $C3(\gamma, \delta)$  map for *Fii* family.

### 4.2.2 $C3(\gamma)$ for given $\delta$

Figures from 4.18 to 4.29 show the values for the maximum achievable characteristic energy  $C3$  with varying flight-path angle  $\gamma$ , for fixed values of declination ( $\delta = [0\ 30\ 45\ 60\ 80]$ ).  $A$  to  $C$  families clearly show the aforementioned periodicity, while last families are subject to the inconsistency presented above, in section 4.2.1. Not only do the curves show irregularities, but also feature inversions that were not expected – meaning that  $C3$  associated to a given delta dip below the equivalent curve for higher declination. As a matter of fact, figures from 4.18 to 4.23 suggest that, for a given  $\gamma$ ,  $C3_{max}$  should decrease with increasing declination: the more the desired escape tends to depart from the ecliptic plane, the smaller the magnitude of the escape velocity that can be achieved.

#### $Aoi - Aii$

Figures 4.18 and 4.19 clearly show the features that have been described in section 4.2.1:  $A$  families have a peak  $C3$  close to  $\gamma = 70^\circ$ , slightly higher for the outbound-inbound family. Moreover, it is also evident how escape manoeuvres are possible only for low declination over the ecliptic plane. For example,  $\delta \geq 45^\circ$  is not achievable if an escape associated to a moon-to-moon leg of  $\sim 1$  month is desired, and even for  $\delta = 30^\circ$  escape trajectories are possible only for a limited range of flight-path angle.

A peculiar feature of the curve for  $\delta = 0^\circ$  is its amplitude: while  $Aoi$  shows a higher peak, it also dips to  $1\ km^2/s^2$ , whereas for  $Aii$  it does not reach  $2\ km^2/s^2$  but it does not fall below  $1.5\ km^2/s^2$ . Thus,  $Aii$  family appears to provide a more consistent escape for any given flight-path angle.

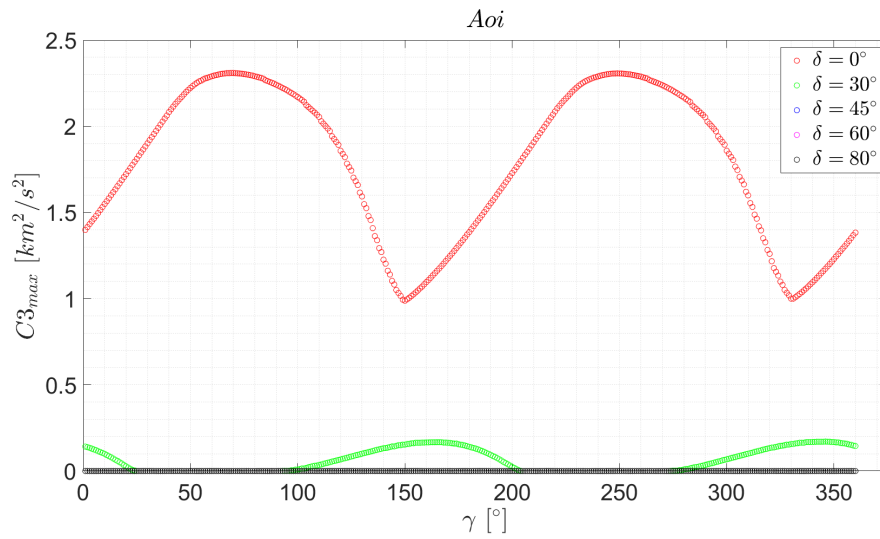


Figure 4.18:  $C3_{max}$  function of the flight-path angle ( $\gamma$ ) for fixed values of declination ( $\delta$ ), Aoi family.

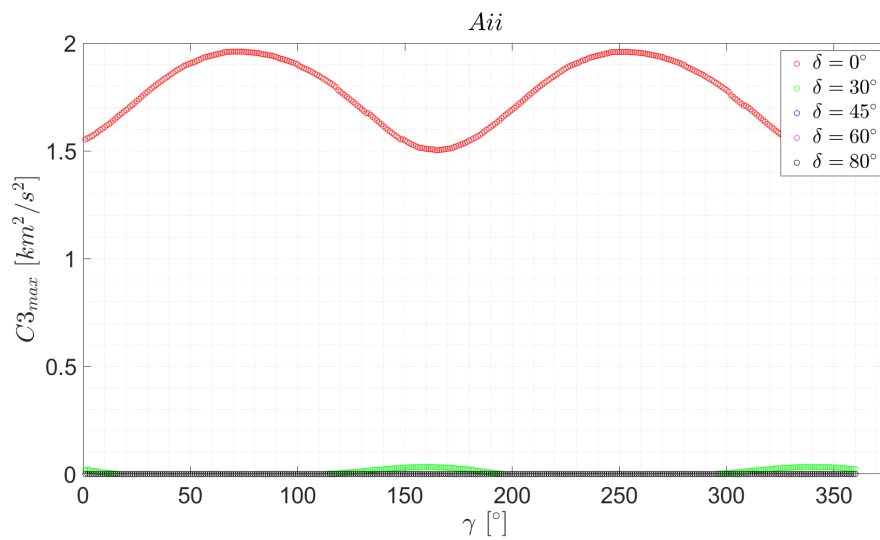


Figure 4.19:  $C3_{max}$  function of the flight-path angle ( $\gamma$ ) for fixed values of declination ( $\delta$ ), Aii family.

*Boi – Bii*

The double peaks described in section 4.2.1 are clearly visible in figures 4.20 and 4.21. *Boi* is continuous between the two peaks, showing a discontinuity for  $\gamma \simeq 120^\circ$ , whereas *Bii* presents a jump both for  $\gamma \simeq 120^\circ$  and for  $\gamma \simeq 55^\circ$ , between the maximums.

Furthermore, it can be noted how the decrease of *C3* with  $\delta$  is more evident moving towards flight-path angles corresponding to the maximums of the curves, while the variation is much more limited when in the range of values of  $\gamma$  associated with minimum *C3*.

Additionally, it can be observed how multiple peaks are present only for  $\delta = 0^\circ$ , whereas higher declination is met with a single maximum. Another characteristic displayed by the maximums is a shift towards smaller flight-path angles: considering *Boi*, while the peak for *C3*( $\delta = 30^\circ$ ) is associated with  $\gamma \simeq 200^\circ$ , the one for  $\delta = 60^\circ$  is before  $\gamma = 180^\circ$ .

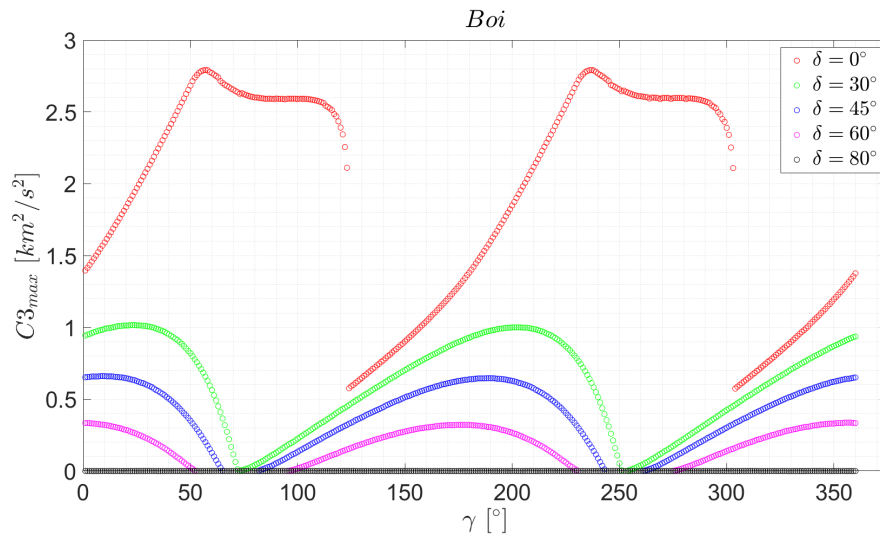


Figure 4.20:  $C3_{max}$  function of the flight-path angle ( $\gamma$ ) for fixed values of declination ( $\delta$ ), *Boi* family.

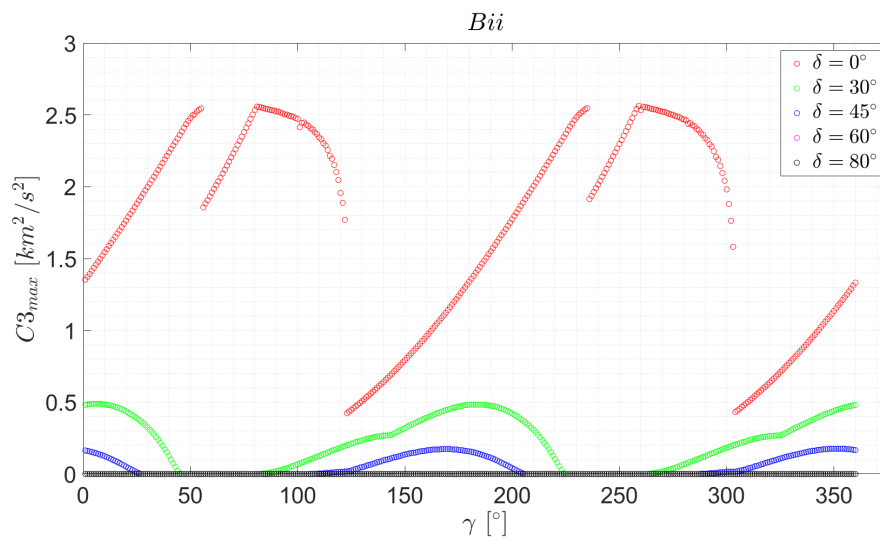


Figure 4.21:  $C3_{max}$  function of the flight-path angle ( $\gamma$ ) for fixed values of declination ( $\delta$ ), *Bii* family.

*Coi – Cii*

*C* families display even better how the minimum values for *C3* are similar for any given  $\delta$ , while the peaks are more spaced out. Similarly to *Boi*, the multiple peaks that appear for null declination do not reach the same value, since the second one is more than  $0.3 \text{ km}^2/\text{s}^2$  below the first one.

It is also evident how the distance between the maximum *C3* for *Coi* and *Cii* is reduced compared to *B* families – and even more if *A* families are taken into account.

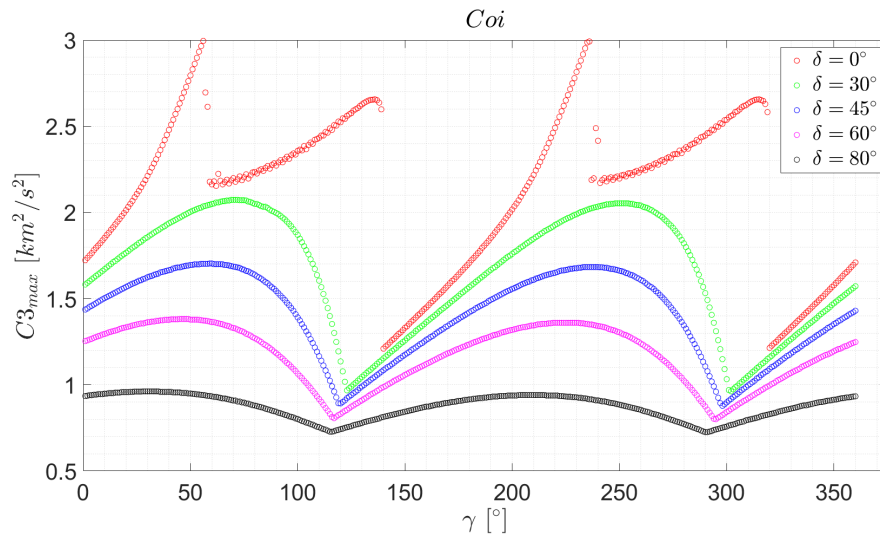


Figure 4.22:  $C3_{max}$  function of the flight-path angle ( $\gamma$ ) for fixed values of declination ( $\delta$ ), *Coi* family.

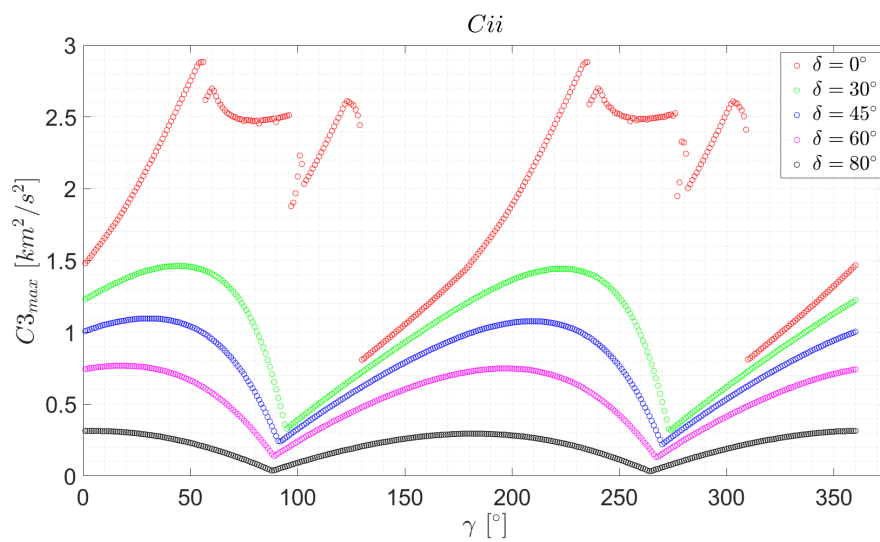


Figure 4.23:  $C3_{max}$  function of the flight-path angle ( $\gamma$ ) for fixed values of declination ( $\delta$ ), *Cii* family.

*Doi – Dii*

Figures 4.24 and 4.25 clearly show the discrepancies and irregularities mentioned in section 4.2.1. While less apparent for  $\delta = 0^\circ$ , higher declination angles see curves for *C3* with multiple discontinuities and jumps, due to a shift from an encounter for a value of  $\theta_S$  to another close to the first one – there is a series of re-encounters for similar conditions, and there is a shift from one to another with varying  $\gamma$ . Moreover, the aforementioned inversions are here displayed: considering for example *Doi* family, between  $\gamma = 60^\circ$  and  $\gamma = 80^\circ$  *C3*( $\delta = 0^\circ$ ) dips below the curve for  $\delta = 60^\circ$ , similarly to the one for  $\delta = 45^\circ$ .

Periodicity itself is broken, which leads to the already introduced hypothesis that the observed behaviour is due to having missed some spacecraft-moon rendezvous.

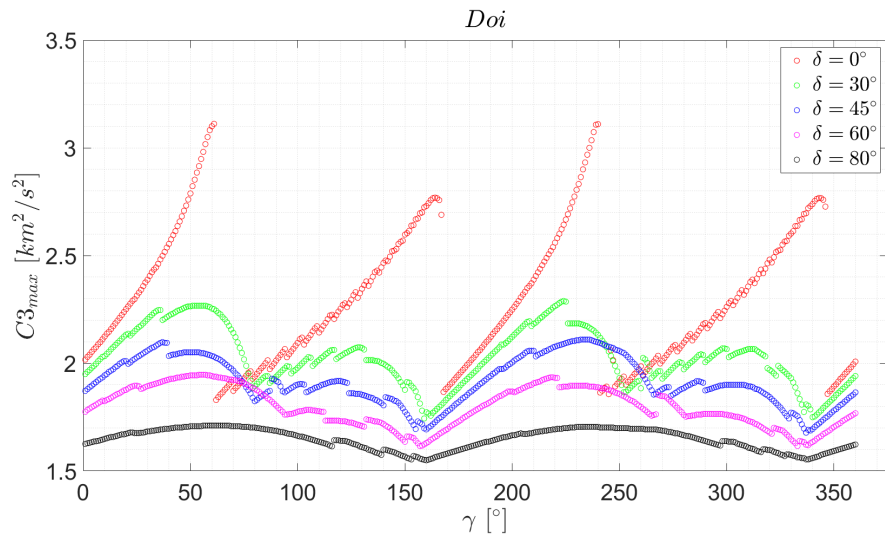


Figure 4.24:  $C3_{max}$  function of the flight-path angle ( $\gamma$ ) for fixed values of declination ( $\delta$ ), *Doi* family.

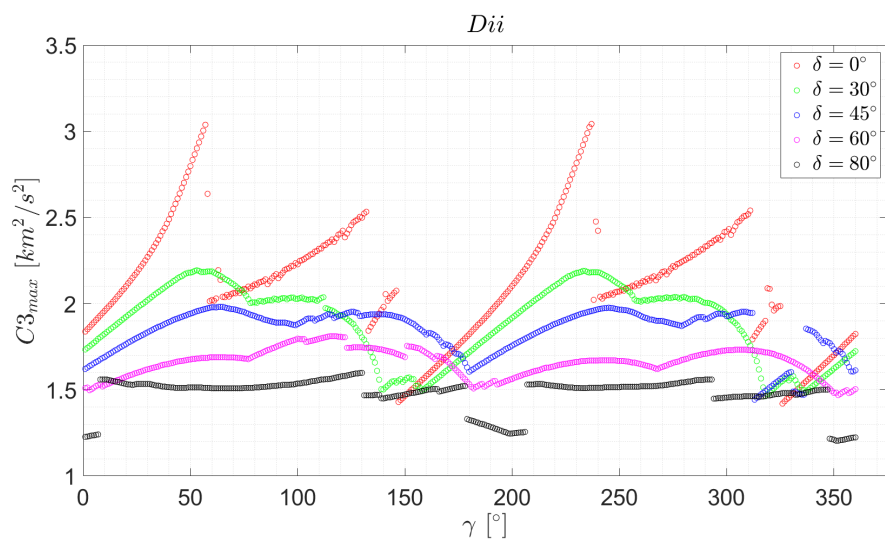


Figure 4.25:  $C3_{max}$  function of the flight-path angle ( $\gamma$ ) for fixed values of declination ( $\delta$ ), *Dii* family.

*Eoi* – *Eii*

*E* families highlight the same trend described above. The difference between the outbound-inbound peak and the inbound-inbound one is reduced to the minimum, as both achieve  $C3 \simeq 3.2 \text{ km}^2/\text{s}^2$  – with *Eii* just slightly inferior.

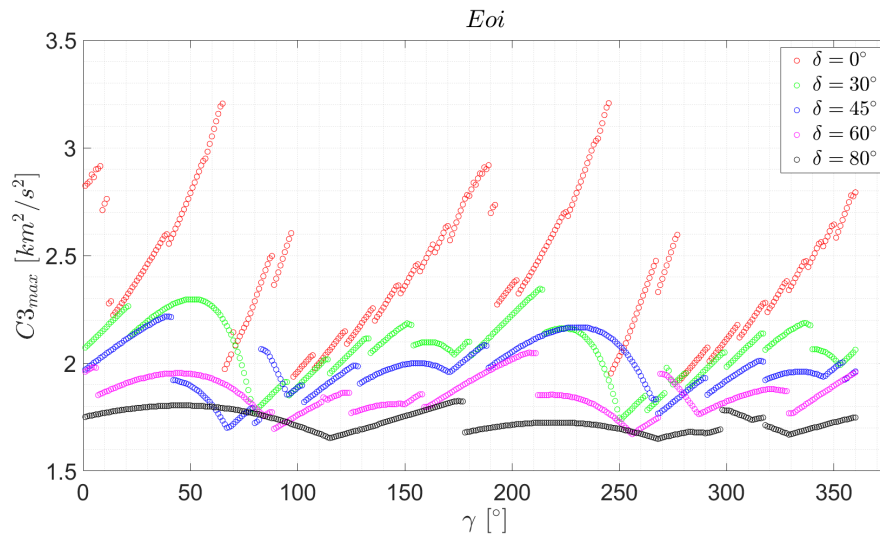


Figure 4.26:  $C3_{max}$  function of the flight-path angle ( $\gamma$ ) for fixed values of declination ( $\delta$ ), *Eoi* family.

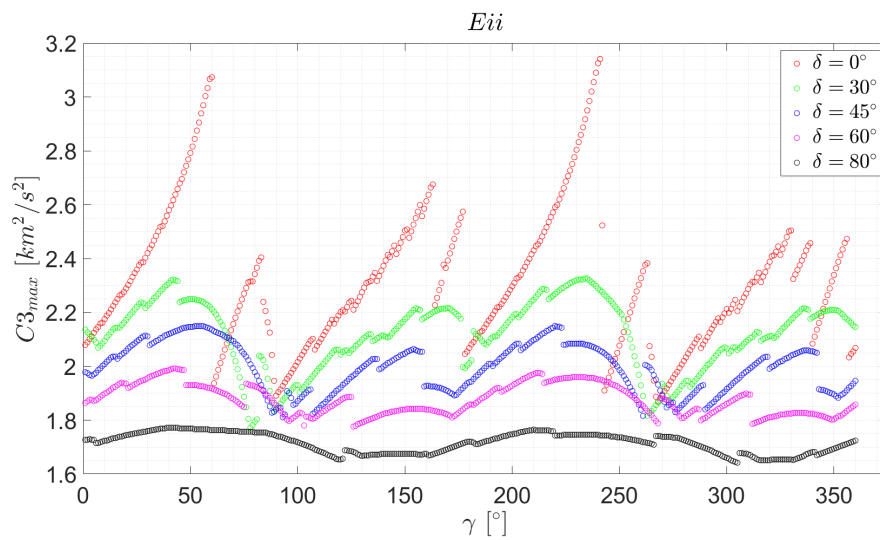


Figure 4.27:  $C3_{max}$  function of the flight-path angle ( $\gamma$ ) for fixed values of declination ( $\delta$ ), *Eii* family.

*Foi – Fii*

The irregularities that were evident for *D* and *E* families are here even more so, with the curve for  $\delta = 30^\circ$  dipping well below that for  $\delta = 80^\circ$ , both for *Foi* and *Fii*. The numerous discontinuities notwithstanding, the trend for the different curves is still perceivable, and it can be observed, ignoring the most prominent dips, how the minimum *C3* is increased when compared to the first families, meaning that escapes that exploit a 6-month long moon-to-moon leg are generally more energetic than quicker ones.

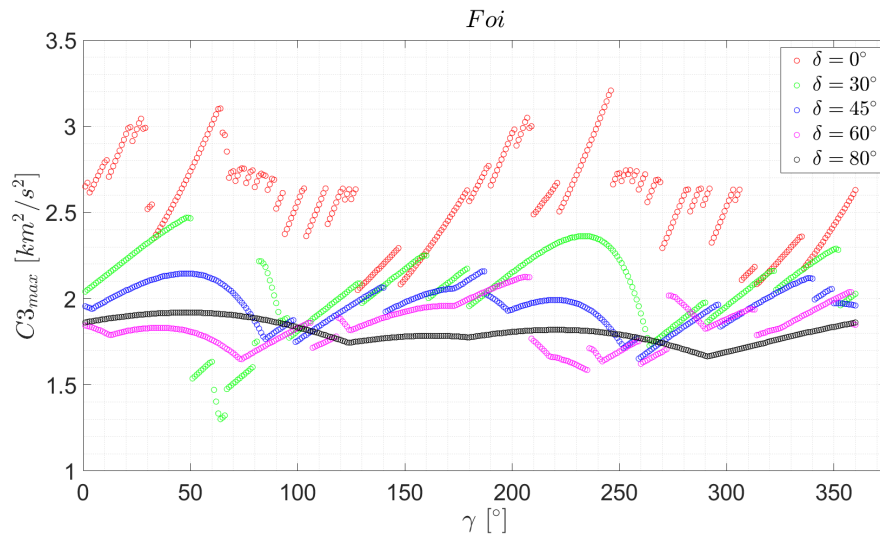


Figure 4.28:  $C3_{max}$  function of the flight-path angle ( $\gamma$ ) for fixed values of declination ( $\delta$ ), *Foi* family.

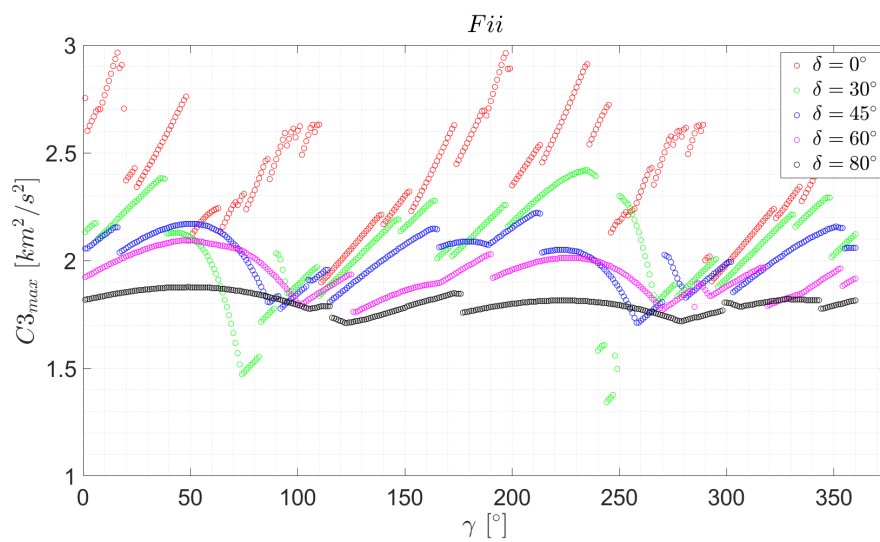


Figure 4.29:  $C3_{max}$  function of the flight-path angle ( $\gamma$ ) for fixed values of declination ( $\delta$ ), *Fii* family.

### 4.2.3 Global results

As mentioned in section 3.2.2, a final matrix, resulting from having assembled the ones for each family, has been obtained, to evaluate the global achievable effect of the lunar gravity assist, independently from the duration of the moon-to-moon leg used to sort the different families.

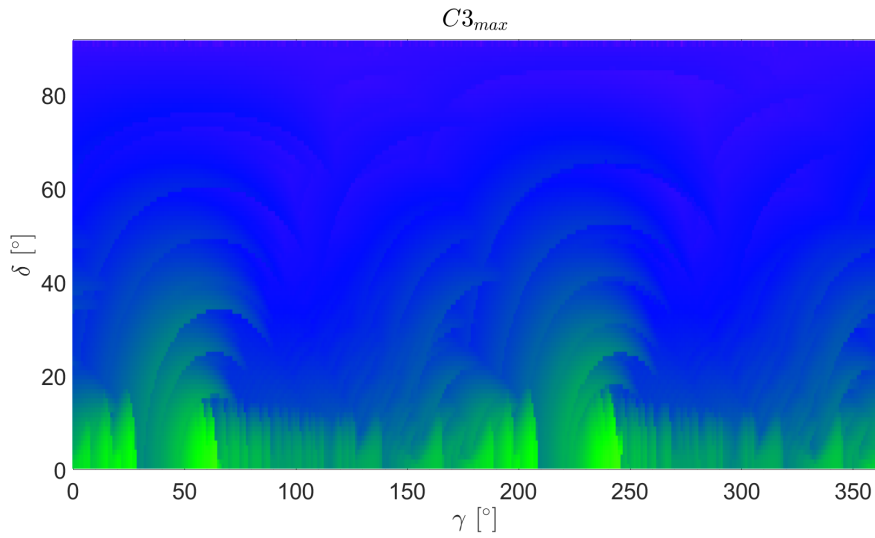
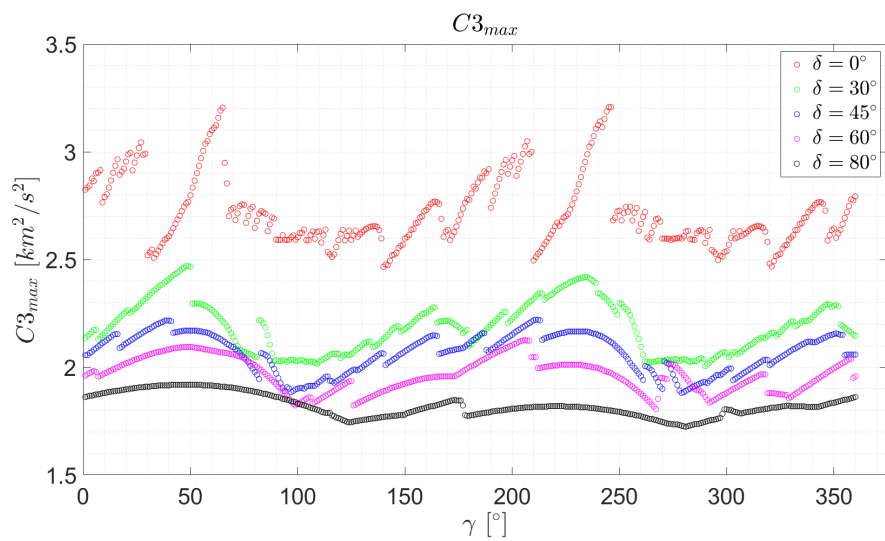
Similarly to what has been done for each family, this matrix has been graphically represented exploiting the same colour scale as before, and the identified behaviour of  $C3(\gamma)$  for the same given values of  $\delta$  has been plotted.

Two major peaks can be identified: the first, smaller, one is located in the proximity of flight-path angle  $\gamma = 30^\circ$ , and it reaches up to the value of  $C3 = 3.04 \text{ km}^2/\text{s}^2$  for a declination of  $\delta = 0^\circ$  – corresponding to the first peak of the *Foi* family, visible in figure 4.28; the second one, on the other hand, is higher and reaches  $C3 = 3.21 \text{ km}^2/\text{s}^2$  for  $\gamma \simeq 60^\circ$  – corresponding to the first peak of the *Eoi* family or the second one for the *Foi* one.

As far as the minimum value is concerned, any combination of flight-path angle and declination yields  $C3 \geq 1.5 \text{ km}^2/\text{s}^2$ . This minimum corresponds to  $\gamma = 273^\circ$  and  $\delta = 90^\circ$ , thus it is not totally reliable due to the aforementioned irregularities appearing for high declination and it is likely that the minimum may be higher.

Finally, two additional graphs have been produced (figures 4.32 and 4.33, then merged in figure 4.34), showing the minimum and maximum  $C3$  achievable with varying  $\delta$ , so as to understand what the guaranteed achievable escape velocity given the desired escape declination is.

Although some irregularities are present, carried over by the ones in the single families, the behaviour of the minimum  $C3_{max}$  is definitely clear: lower declination is associated to generally more energetic escapes, since a smaller part of the gained  $\Delta V$  is spent for the rotation of the  $\mathbf{V}$  vector away from the ecliptic plane. With a planar escape –  $\delta = 0^\circ$  – the minimum guar-

Figure 4.30:  $C3_{max}(\gamma, \delta)$ .Figure 4.31:  $C3_{max}$  function of the flight-path angle ( $\gamma$ ) for fixed values of declination ( $\delta$ ).

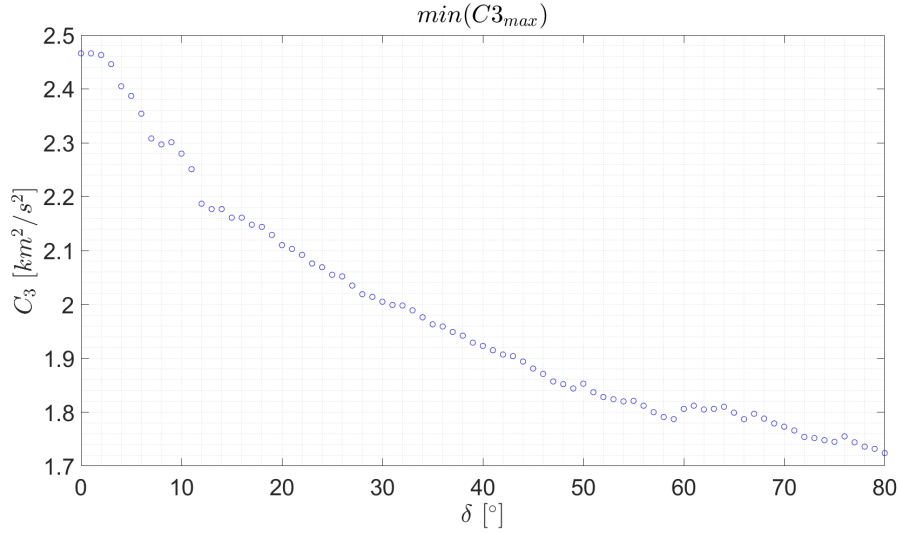


Figure 4.32: Minimum  $C3_{max}(\gamma)$  varying with  $\delta$ .

anted escape velocity, independent from the desired flight-path angle, is  $V_{esc} = 1.57 \text{ km/s}$ , as the associated  $C3$  is just shy of  $2.5 \text{ km}^2/\text{s}^2$ , reaching  $2.47 \text{ km}^2/\text{s}^2$ . This value stays relatively stable until  $\delta = 2^\circ$ , where it starts to rapidly decline, shifting to  $C3 \simeq 2.18 \text{ km}^2/\text{s}^2$  for  $\delta = 12^\circ$ ; after that, the steepness of the descent diminishes and, for  $\delta = 80^\circ$ ,  $C3 \simeq 1.7 \text{ km}^2/\text{s}^2$  is achieved. Higher declination has not been considered in this part of the analysis, due to the aforementioned irregularities found in that region.

Figure 4.33 shows a similar behaviour for the maximum values for  $C3$ : starting from  $C3 = 3.21 \text{ km}^2/\text{s}^2$ , the decrease gets faster and faster up to  $\delta = 15^\circ$ , where it stabilizes and, even though with minor irregularities, proceeds steadily up to  $C3 \simeq 1.9 \text{ km}^2/\text{s}^2$  for  $\delta = 80^\circ$ .

The combination of the two curves presented in figure 4.34 shows how the greatest variation in achievable escape velocity is associated with planar escape trajectories, for which  $\Delta C3_{max} = 0.74 \text{ km}^2/\text{s}^2$ . With the increase of the desired escape declination, not only does the achievable characteristic energy decrease, but the range of maximum  $C3$  decreases as well, shifting to  $\Delta C3_{max} \simeq 0.2 \text{ km}^2/\text{s}^2$  for  $\delta = 80^\circ$ .

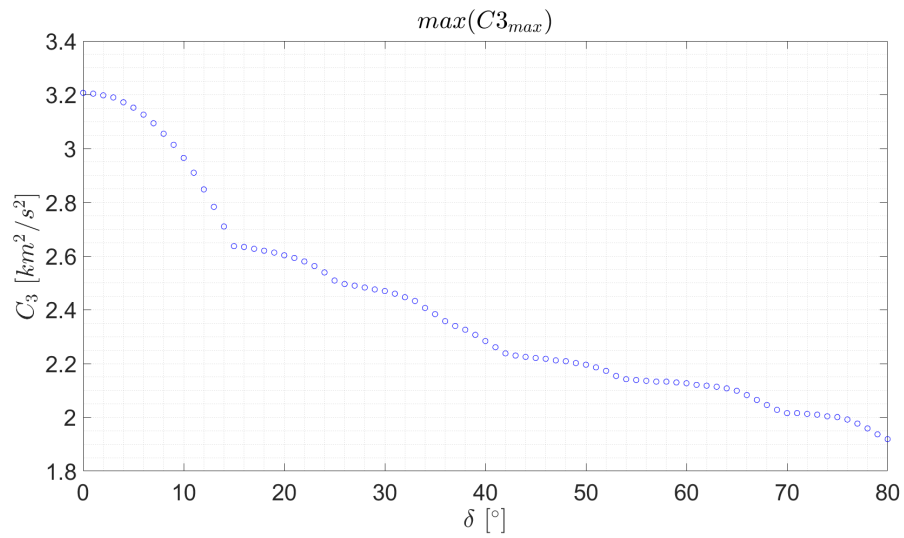


Figure 4.33: Maximum  $C3_{max}(\gamma)$  varying with  $\delta$ .

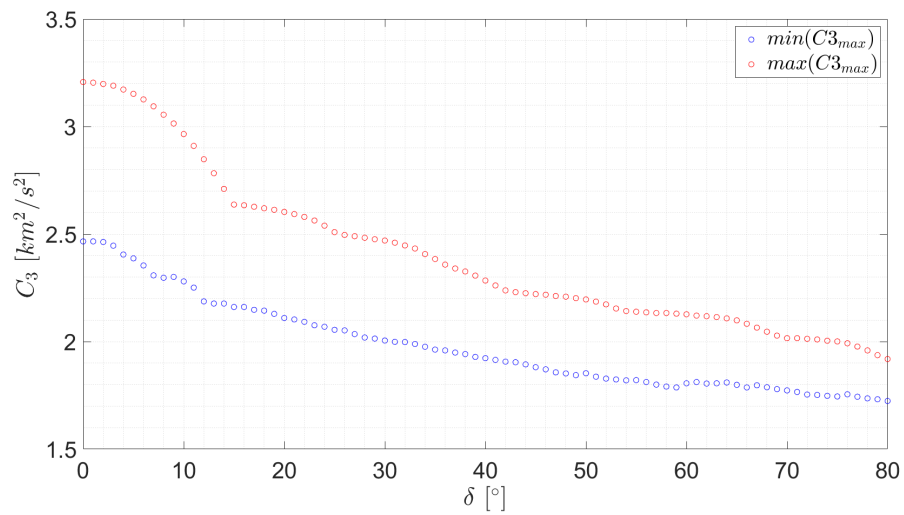


Figure 4.34: Minimum and maximum  $C3_{max}(\gamma)$  varying with  $\delta$ .



# Chapter 5

## Conclusions

### 5.1 Conclusions

The aim of the present study was to investigate the possibilities of multiple lunar gravity assist-aided escape manoeuvres, identifying the correlation between the desired escape conditions, in terms of heliocentric flight-path angle and declination, and the achievable escape velocity, expressed as the square root of the specific characteristic energy  $C3$ . First, the solar-perturbed orbits allowing two consecutive LGAs have been discussed, through the presentation of the algorithm developed to identify them, using as starting conditions a plausible result of a gravity assist manoeuvre. Then, the second LGA has been studied for each moon-to-moon transfer found in the previous section. The resulting data, linking heliocentric flight-path angle, declination and the associated  $C3$  at the escape to the characteristics of the gravity assist – namely, pump and crank angle – have been interpolated, to directly associate a  $C3$  for each couple  $(\gamma, \delta)$ . Due to the inherent symmetry of the LGA, only the case  $\delta > 0^\circ$  has been considered.

Results show how this escape strategy can be convenient for interplanetary missions, since the heliocentric escape velocity that can be achieved is not dependent on an expended propellant mass. Thus, payload mass can be increased in comparison to thrust-based escape strategies, in exchange for longer mission duration. Moreover, the maps that have been presented can

be used in a preliminary design phase of an interplanetary mission exploiting such escape strategy, since they relate the characteristics of the desired heliocentric orbit to the minimum guaranteed achievable escape velocity.

## 5.2 Future work

The main issue faced during the development of the present study has consisted of the identification of the moon-to-moon legs allowing two consecutive lunar gravity assists. Even forcing the search for the symmetric solution – supposed present due to the inherent symmetry of the solar perturbation acting during orbit propagation – has not eliminated the irregularities that have been discussed in sections 4.2.1 and 4.2.2, even though it definitely limited them and allowed the visualization of the general behaviour of the curves. Thus, the present work might be complemented by an additional study focused on the research on the missing solutions.

Furthermore, the study might be repeated with different starting conditions, namely the initial spacecraft velocity relative to the moon's, to widen the spectrum of the produced maps.

Finally, the present work might be complemented by an analysis of the launch and Earth-to-moon phases, to complete the evaluation of the geocentric part of an interplanetary mission.

# Acknowledgements

I would first like to thank my mentor prof. Lorenzo Casalino for his invaluable assistance during the development of this thesis, as his help stretched far over what would be expected of a thesis advisor. I would also like to thank prof. Michèle Lavagna of Politecnico di Milano for her kind availability to cover the role of co-supervisor during the months of preparation of this study.

I would also like to acknowledge my friends and colleagues Emanuele Sanguineti, Filippo Corradino, Francesco Santacroce and Susanna Orestano, that helped me overcome some critical moments during this work.

Finally, I must express my gratitude to my parents, who constantly supported me during all these years. This accomplishment would not have been possible without them. Thank you.



# Bibliography

- [1] Roger R Bate, Donald D Mueller, and Jerry E White. *Fundamentals of astrodynamics*. Courier Corporation, 1971.
- [2] Lorenzo Casalino and Lucio Filizola. “Design of High-Energy Escape Trajectories with Lunar Gravity Assist”. In: *26th International Symposium on Space Flight Dynamics*. ISTS. 2017.
- [3] Lorenzo Casalino and Gregory Lantoine. “Design of Lunar-Gravity-Assisted Escape Maneuvres”. In: *2017 AAS/AIAA Astrodynamics Specialist Conference*. AAS/AIAA. Aug. 22, 2017.
- [4] Lucio Filizola. “Escape trajectories toward near-Earth asteroids exploiting multiple Lunar gravity assists”. Master thesis. Politecnico di Torino, 2017.
- [5] Wang Sang Koon et al. “Low energy transfer to the Moon”. In: *Dynamics of Natural and Artificial Celestial Bodies*. Springer, 2001, pp. 63–73.
- [6] Gregory Lantoine and Timothy P McElrath. “Families of Solar-perturbed moon-to-moon transfers”. In: *24th AAS/AIAA Spaceflight Mechanics Meeting*. AAS/AIAA. 2014.
- [7] Timothy P McElrath et al. “Using gravity assists in the Earth-Moon system as a gateway to the solar system”. In: *Global Space Exploration Conference (GLEX) 2012* (2012).
- [8] Isaac Newton. *The Principia: mathematical principles of natural philosophy*. Univ of California Press, 1999.

- [9] Hanspeter Schaub and John L Junkins. *Analytical mechanics of space systems*. Aiaa, 2003.
- [10] David R Williams. *Moon Fact Sheet*. Ed. by NASA. July 3, 2017. URL: <https://nssdc.gsfc.nasa.gov/planetary/factsheet/moonfact.html>.